

Imperial College London
Department of Earth Science and Engineering

The Limitations of Acoustic Full-Waveform Inversion in an Elastic World

George Strong
2018

Supervised by Prof. Michael Warner

Disclaimer

This report is submitted as part requirement for the MSci Degree in Geophysics at Imperial College London. It is substantially the result of my own work except where explicitly indicated in the text. The report may be freely copied and distributed provided the source is explicitly acknowledged.

George Strong

The main body of this dissertation has 5374 words.

Abstract

The limitations of acoustic full-waveform inversion (FWI) are evaluated with particular reference to a North Sea case study: the Buzzard Field. As most efficient three-dimensional FWI algorithms are based on the acoustic wave equation, they do not correctly account for elastic effects. The acoustic approximation results in the seemingly unpredictable failure of acoustic FWI on certain data sets, including on the Buzzard field data set. The criteria for these failures have been evaluated through the development of a comprehensive code for modelling reflection and transmission coefficients in anisotropic elastic media using Zoeppritz equations. The code was implemented within Monte Carlo simulations in order to fully investigate the parameter space and was then used to generate Kirchhoff synthetic seismograms in order to model the reflected wavefield.

This approach was successful in pinpointing the phenomena that caused the failure of FWI on the Buzzard Field data set, demonstrating that problems arise due to the presence of a shallow chalk formation which results in large P and S-wave velocity contrasts of 2000ms^{-1} and 1700ms^{-1} respectively. More precisely, the failure was found to be a consequence of elastic effects originating from the top-chalk interface at a depth of 1000m, reducing the post-critical P-wave reflection coefficients by 90% relative to the acoustic case. The top-chalk post-critical reflection coefficients were also found to be highly sensitive to weak anisotropy within the reflecting medium (the chalk) and are reduced by more than 80% relative to the isotropic case when the chalk anisotropy satisfies $\varepsilon - \delta \geq 0.2$. Acoustic modelling does not fully account for these anisotropic effects, even when the elastic effects are negligible. It was therefore hypothesized that acoustic FWI will not correctly handle data sets that contain a shallow interface with high P-wave velocity contrasts if there is also a significant S-wave velocity contrast, or if the anisotropy of the reflecting medium satisfies $\varepsilon - \delta \geq 0.2$. These discoveries could indicate where similar failures on other comparable examples could be found, either prior to running acoustic FWI or after a failure on a data set, with the results highlighting the growing need for elastic FWI or methods for mitigating elastic effects within acoustic FWI in the future.

Contents

	Page
1 Introduction	5
2 Background	6
2.1 Full-Waveform Inversion	6
2.2 Buzzard Field Data Set	7
2.3 Buzzard FWI Results	8
3 Methodology	11
3.1 Isotropic Zoeppritz Equations	12
3.2 Anisotropic Zoeppritz Equations	13
3.2.1 Incident Slowness Vectors	13
3.2.2 Reflected and Transmitted Slowness Vectors	14
3.2.3 Polarization Vectors	15
3.2.4 Reflection and Transmission Coefficients	15
3.3 Buzzard Parameter Estimation	18
3.4 Monte Carlo Simulations	20
4 Results	21
4.1 Zoeppritz Modelling Code	21
4.1.1 Functionality	21
4.1.2 Development	21
4.2 Buzzard Zoeppritz Modelling	24
4.3 Buzzard Monte Carlo Simulations	25
4.3.1 Isotropic Simulation	25
4.3.2 Anisotropic Simulations	26
5 Discussion	28
5.1 Kirchhoff Synthetic Seismogram	28
5.2 Elastic Effects	30
5.3 Anisotropic Effects	32
6 Conclusion	35

Appendix A Codes	39
A.1 ZMC: Key Sections	39
A.1.1 Incident Slowness Vectors	39
A.1.2 Reflected/Transmitted Slowness Vectors	40
A.1.3 Polarization Vectors	41
A.1.4 Reflection and Transmission Coefficients	42
A.1.5 Solver	44
A.2 Isotropic Zoeppritz Matrix Equation	45
A.3 Kirchhoff Synthetic Seismogram	46
Appendix B Additional Figures	48
B.1 Contractors' Anisotropy Model	48
B.2 FWI Synthetics	49
B.3 Acoustic Modelling of Anisotropic Effects	50

List of Figures

	Page
1 Buzzard FWI Starting and Recovered P-wave Velocity Models	8
2 Buzzard Common Image Gather	9
3 Buzzard Field Data and Acoustic Synthetic	10
4 Resolved Instabilities in Phase and Reflection Coefficients	23
5 Buzzard P-wave Reflection Coefficient Profiles	24
6 Isotropic Elastic Monte Carlo Simulation	25
7 Anisotropic Clastic Unit Monte Carlo Simulation	26
8 Fully Anisotropic Monte Carlo Simulation	27
9 Kirchhoff Synthetic Seismograms	29
10 F-K Filtered Buzzard Field Data and Acoustic Synthetic	31
11 HTI Anisotropic Monte Carlo Simulations	33
12 Contractors' VTI Anisotropy Model	48
13 FWI Synthetics	49
14 Acoustic Modelling of Anisotropic Effects	50

List of Tables

	Page
1 Buzzard Survey Acquisition Parameters	7
2 Buzzard Parameter Estimations	19
3 Zoeppritz Modelling Code Validation	22

1 Introduction

Full-waveform inversion (FWI) is a computational method for generating high-resolution, quantitative models of the subsurface (Warner et al. 2013). The use of FWI is standard practice within the oil industry and is typically successful if there is a good starting model, quality assurance and a suitable field data set containing low-frequencies, long-offsets and sufficient penetration depths of turning arrivals (Warner et al. 2013). However, most efficient three-dimensional FWI algorithms use the acoustic wave equation, which does not correctly account for elastic effects, such as P to S phase conversions (Warner et al. 2013). This is due to the computational cost and additional complexities that accounting for elastic effects incurs (Warner et al. 2013, Agudo et al. 2016). The aim of this project is to investigate a seismic data set where acoustic FWI fails, using plane-wave reflection coefficients. To do this, I have developed a comprehensive code for modelling reflection and transmission coefficients in anisotropic elastic media using the Zoeppritz equations, with the additional aim for it to be used by others for different purposes.

2 Background

2.1 Full-Waveform Inversion

The three-dimensional wave equation can be used to generate synthetic seismic data from a velocity model (Warner et al. 2013). This can be expressed as

$$\mathbf{G}(\mathbf{m}) = \mathbf{p} \quad (1)$$

where \mathbf{m} is the P-wave velocity model, \mathbf{p} is the synthetic seismic data and \mathbf{G} is a function that represents the numerical implementation of the wave equation for a given source wavefield and acquisition geometry (Warner et al. 2013). The aim of FWI is to recover an unknown model, \mathbf{m}' , from an observed seismic data set, \mathbf{d} , which can be represented as

$$\mathbf{m}' = \mathbf{G}^{-1}(\mathbf{d}). \quad (2)$$

Solving equation 2 directly is not possible, due to the non-linear relationship between the model and the seismic data: \mathbf{G} is not a matrix and therefore has no formal inverse (Warner et al. 2013). In order to proceed, FWI assumes a starting model, \mathbf{m}_0 , that is relatively close to the true model \mathbf{m}' (Warner et al. 2013). It then iteratively updates the starting model with small perturbations, $\delta\mathbf{m}$, so that the misfit between the observed data and the synthetic data is minimised (Warner et al. 2013). The misfit is defined by the objective function f , of the form

$$f(\mathbf{m}) = \frac{1}{2} \|\mathbf{d} - \mathbf{p}\|_2^2. \quad (3)$$

A linear relationship can be assumed between the small model perturbations, $\delta\mathbf{m}$, and the corresponding perturbations in the difference between the observed and synthetic data, $\mathbf{d} - \mathbf{p}$ (Warner et al. 2013). The solution for $\delta\mathbf{m}$ can then be expressed as

$$\delta\mathbf{m} = -\mathbf{H}^{-1} \frac{\partial f}{\partial \mathbf{m}} \quad (4)$$

where \mathbf{H} is the Hessian operator, containing all the second-order differentials of the objective function (Warner et al. 2013). As the Hessian contains an extremely large number of elements, an approximate Hessian is used instead, keeping only its diagonal components (Warner et al. 2013). The gradient, $\partial f / \partial \mathbf{m}$, is determined by back-propagating the residual between the observed and synthetic data at the receivers into the model (Tarantola 1984). This is then cross-correlated with the forward wavefield for every point in the model (Tarantola 1984). Refer to Virieux & Operto (2009) for a more comprehensive account of FWI theory.

2.2 Buzzard Field Data Set

The field data for this study was taken from the Buzzard Field in the North Sea and was supplied by Nexen Petroleum U.K. Limited. The Buzzard Field is situated at the western margin of the Ettrick Sub-basin and is 100km north-east of Aberdeen in the Outer Moray Firth, UK North Sea, Blocks 19/10, 20/6, 19/5aS and 20/1S (Seabed-Geosolutions 2014). The reservoir is composed of Upper Jurassic deep marine turbidites within the Kimmeridge Clay Formation, located at a depth of 2380m (Ray et al. 2011, Doré & Robbins 2005). Above this is the Valhall formation, comprised of interbedded sandstones and mudstones, followed by a 500m thick chalk formation (Doré & Robbins 2005). A sharp unconformity defines the top of this formation (the Chalk Group), separating it from a 1000m thick unit of various younger clastic rocks that stretch to the seafloor, referred to in this study as the Clastic Unit (Doré & Robbins 2005).

In 2014, a high-density, three-dimensional ocean-bottom-node survey was acquired with the aim to update and enhance the geological simulation models of the Buzzard Field (Seabed-Geosolutions 2014). The ocean-bottom-nodes were deployed in two zones: an outer zone with a $300\text{m} \times 300\text{m}$ receiver layout, and a dense inner core with a $150\text{m} \times 150\text{m}$ receiver layout (Seabed-Geosolutions 2014). Also, full fold coverage extends to a minimum of 3000m (Seabed-Geosolutions 2014). Refer to Table 1 for details of the acquisition parameters.

Receiver Parameters	
No of OBN Locations	1293
OBN Area	87000m^2
Outer OBN Cross/In-line Spacing	300m
Inner OBN Cross/In-line Spacing	150m
Seawater Depth	100m

Source Parameters	
Source Type	Dual airgun array, flip-flop shooting
Airgun Size	2980in^3
Source Depth	6m
No of Shots	389426
Shot Area	243000m^2
Source Line Azimuth	$093/273^\circ$
Source Line Length	Various
Source Cross-line Separation	25m
Source In-line Separation	12.5m

Table 1: Receiver and source parameters used by Seabed-Geosolutions (2014) in the acquisition of the Buzzard OBN field data set.

2.3 Buzzard FWI Results

Anisotropic three-dimensional acoustic FWI was conducted on the Buzzard hydrophone data by Prof M. Warner. A reverse time migrated P-wave velocity model, provided by the contractor, was used as the FWI starting model and is shown in Figure 1. The anisotropy model (ε and δ/ε) used in the inversion was also provided by the contractor (see Appendix B.1). The recovered FWI P-wave velocity model, also shown in Figure 1, was generated using initial and final frequencies of 3Hz and 10Hz respectively.

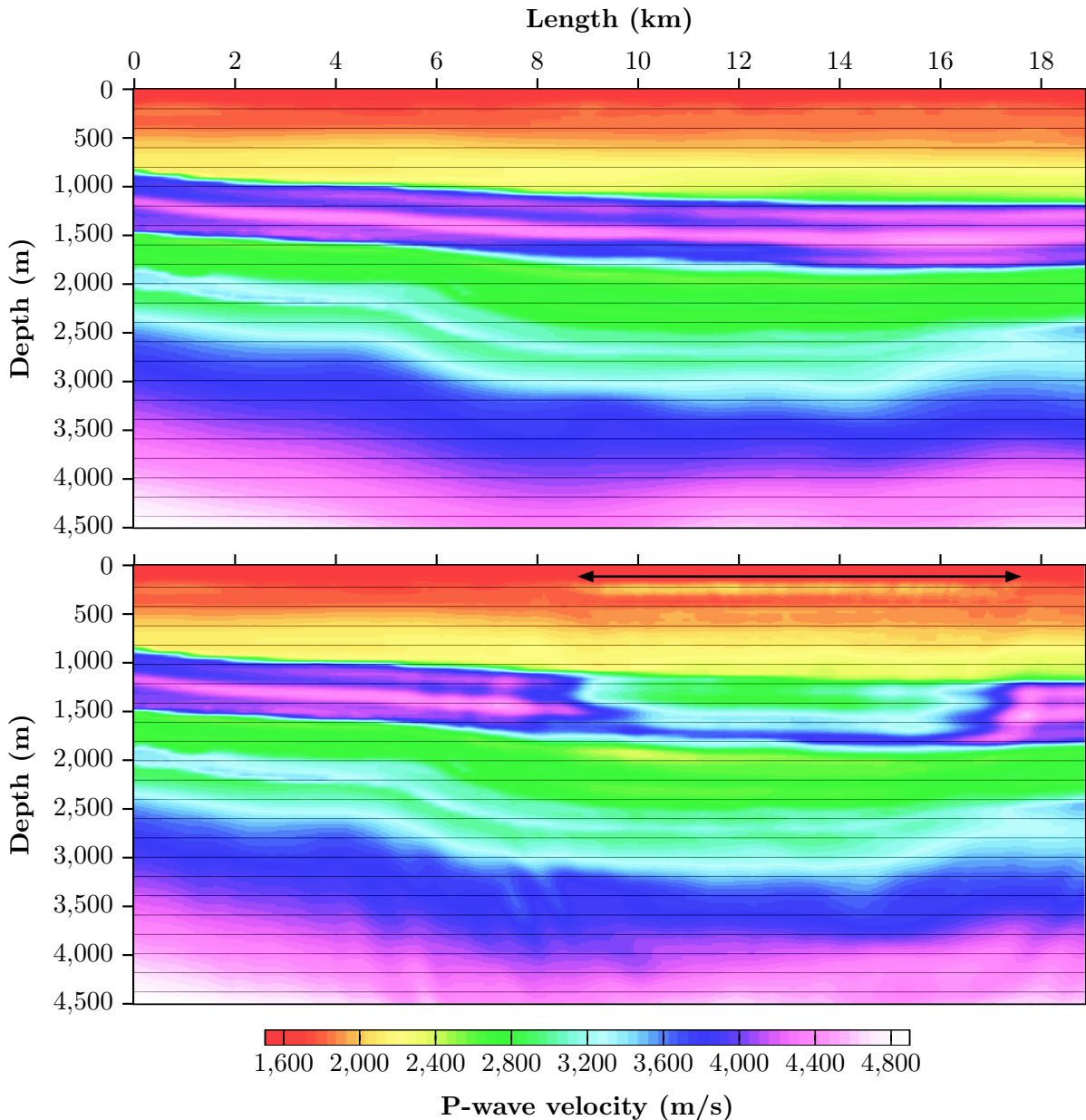


Figure 1: Top: FWI starting P-wave velocity model. Bottom: recovered FWI P-wave velocity model. The arrow indicates the location of live data used in this study. Note the significant reduction in velocity of the Chalk Group (located at 1000m to 1700m depth) in the FWI model.

FWI has aggressively suppressed the P-wave velocity of the Chalk Group, reducing it from 4000ms^{-1} in the starting velocity model to 2500ms^{-1} , as shown in Figure 1. This suggests that the velocity of the chalk in the starting velocity model is incorrect. A PZ-summed common image gather (CIG) was generated by Prof M. Warner, given in Figure 2, to verify the chalk velocity in the starting model. The flattened gathers observed at the base of the chalk in Figure 2 confirm that the P-wave velocity of the Chalk Group cannot be significantly in error. Evidently, FWI is failing to recover an accurate model within the chalk. This is consistent throughout the model, independent of parameterisation, pre-processing and the type of acoustic FWI used.

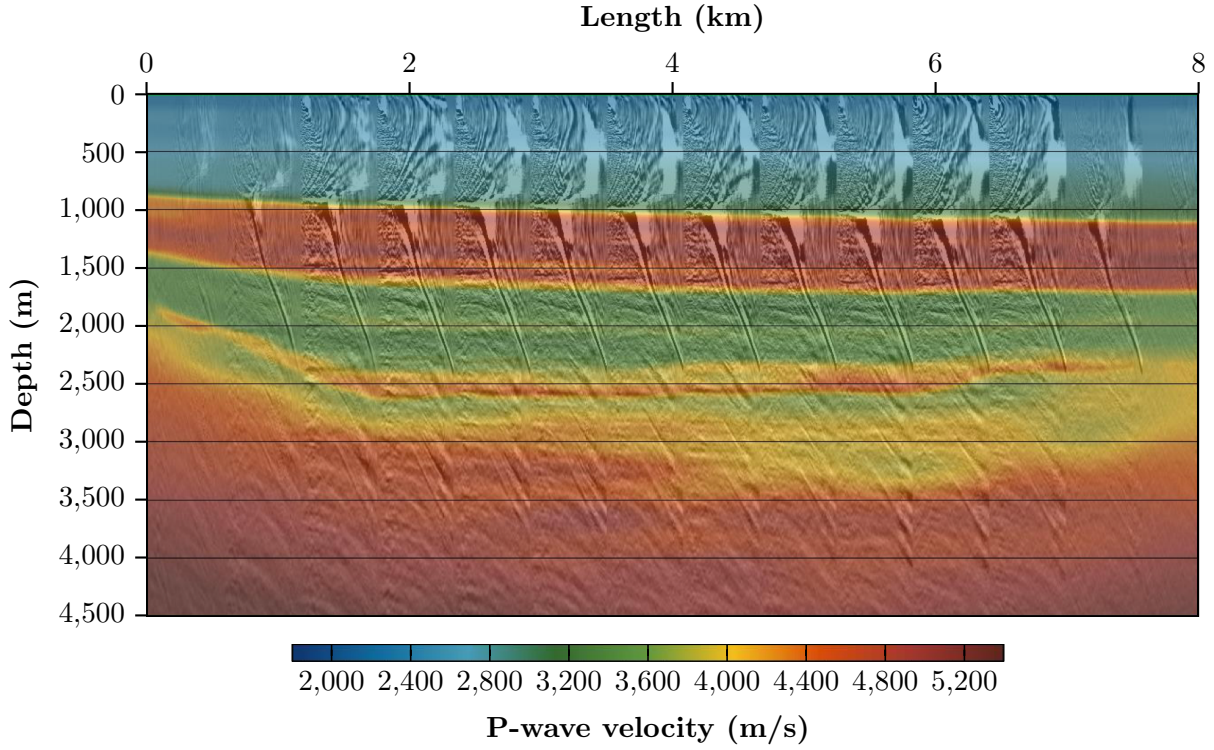


Figure 2: Buzzard PZ-summed common image gather. The flattened gathers at the base of the Chalk Group (1500m) verify the chalk velocity in the FWI starting velocity model.

A shot record of the field data is shown alongside an acoustic synthetic generated from the starting velocity model in Figure 3. The acoustic synthetic contains high amplitude post-critical top-chalk reflections and corresponding 1st, 2nd and 3rd order multiples. These high amplitude events are absent in the field data. In order to reduce the misfit between the synthetic and the field data, FWI suppresses these high amplitude post-critical top-chalk reflections and their multiples by incorrectly obliterating the high P-wave velocity of the chalk. This disparity is caused by phenomena which are consequently ultimately responsible for the failure of FWI on the Buzzard Field data set. A Zoeppritz modelling code for anisotropic elastic media has been developed in order to investigate whether the failure of acoustic FWI is due to the presence of elastic effects and/or complexities in the anisotropy model (in the case that the contractors' anisotropy model is incorrect).

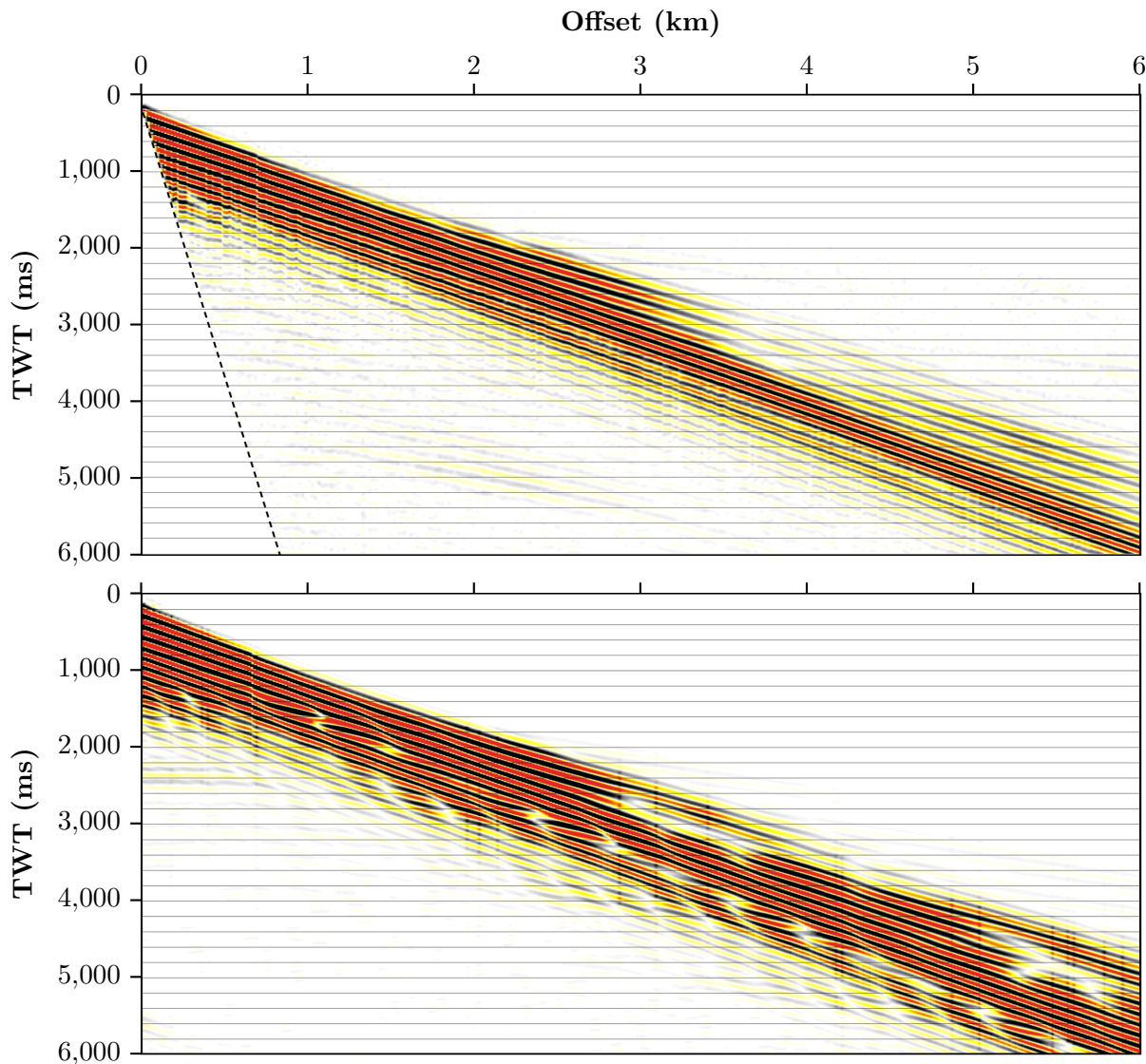


Figure 3: Top: bandpass filtered shot record of the Buzzard field data set, arbitrarily chosen from the middle of the survey. The dotted black line indicates where a mute was applied to remove Scholte waves. Bottom: acoustic synthetic data at the same location as the field data generated using the starting P-wave velocity model. Note the strong post-critical top chalk reflections (well defined at a two-way-time of 1600ms) and their multiples in the acoustic synthetic. These are absent in the field data.

3 Methodology

The Zoeppritz equations govern the proportion of seismic energy that is reflected and transmitted from an interface between two homogenous elastic media (Zoeppritz 1919). They have been used to investigate the proportion of P-wave energy reflected by the top-chalk interface in the Buzzard field data set. The theory presented in this section forms the basis for the development of the Zoeppritz modelling codes used in this project.

The Zoeppritz equations are formulated by assuming the solution to the wave equation (equation 5) takes the form of an elastic plane wave (equation 6) (Zoeppritz 1919).

$$\left(\rho \delta_{ij} \frac{\partial^2}{\partial t^2} - \mathbf{C}_{ikjm} \frac{\partial^2}{\partial x_k \partial x_m} \right) u_j = 0, \quad i = 1, 2, 3, \quad (5)$$

$$u_i = q_i \exp[i\omega(t - s_k x_k)], \quad i = 1, 2, 3, \quad (6)$$

where ρ is the density, δ_{ij} is the Kronecker delta function, \mathbf{C}_{ikjm} is the fourth order elastic tensor, \mathbf{u}_{ij} is the displacement, \mathbf{q}_{ij} is the polarization vector, \mathbf{s}_{km} is the slowness vector and ω is the angular frequency (Keith & Crampin 1977). This yields the following equation (Keith & Crampin 1977):

$$\rho q_i = \mathbf{C}_{ikjm} s_k s_m q_j, \quad i = 1, 2, 3, \quad (7)$$

\mathbf{C}_{ikjm} governs the three-dimensional relationship between stress and strain in a medium (Thomsen 1986). It was condensed into a more convenient second order 6×6 matrix, \mathbf{C}_{ij} , by exploiting its symmetrical properties (Voigt 1910). Equation 7 was then rearranged and expressed as

$$(\mathbf{\Gamma} - \rho \mathbf{I}) \mathbf{q} = 0 \quad (8)$$

where $\mathbf{\Gamma}$ is the 3×3 Christoffel matrix, defined for media with monoclinic symmetry as follows (Schoenberg & Protazio 1990):

$$\begin{aligned} \Gamma_{11} &= C_{11}s_1^2 + C_{66}s_2^2 + C_{55}s_3^2 + 2C_{16}s_1s_2 \\ \Gamma_{22} &= C_{66}s_1^2 + C_{22}s_2^2 + C_{44}s_3^2 + 2C_{26}s_1s_2 \\ \Gamma_{33} &= C_{55}s_1^2 + C_{44}s_2^2 + C_{33}s_3^2 + 2C_{45}s_1s_2 \\ \Gamma_{12} &= \Gamma_{21} = C_{16}s_1^2 + C_{26}s_2^2 + C_{45}s_3^2 + (C_{12} + C_{66})s_1s_2 \\ \Gamma_{13} &= \Gamma_{31} = (C_{13} + C_{55})s_1s_3 + (C_{36} + C_{45})s_2s_3 \\ \Gamma_{23} &= \Gamma_{32} = (C_{36} + C_{45})s_1s_3 + (C_{23} + C_{44})s_2s_3. \end{aligned}$$

Explicit solutions for the reflection and transmission coefficients of incident P and S-waves were then found by imposing continuity of displacement and traction across the interface (Zoeppritz 1919).

3.1 Isotropic Zoeppritz Equations

For the isotropic case, the Zoeppritz equations were expressed in the simple matrix equation form

$$\mathbf{Q} = \mathbf{P}^{-1} \mathbf{R} \quad (9)$$

where \mathbf{Q} is the scattering matrix containing all sixteen reflection and transmission coefficients (Aki & Richards 1980):

$$\mathbf{Q} = \begin{bmatrix} R_{PP}^U & R_{SP}^U & T_{PP}^L & T_{SP}^L \\ R_{PS}^U & R_{SS}^U & T_{PS}^L & T_{SS}^L \\ T_{PP}^U & T_{SP}^U & R_{PP}^L & R_{SP}^L \\ T_{PS}^U & T_{SS}^U & R_{PS}^L & R_{SS}^L \end{bmatrix}.$$

The first letter of each term in \mathbf{Q} represents whether it is a reflection (R) or transmission (T) coefficient. The two subscript letters denote first, the type of incident and second, reflected/transmitted waves. ^U and ^L denote whether the incident wave is arriving in the upper or lower medium (Aki & Richards 1980). Matrices \mathbf{P} and \mathbf{R} are defined as follows:

$$\mathbf{P} = \begin{bmatrix} -\sin\theta_1 & -\cos\phi_1 & \sin\theta_2 & \cos\phi_2 \\ \cos\theta_1 & -\sin\phi_1 & \cos\theta_2 & -\sin\phi_2 \\ 2\rho_1 V_{S1} \sin\phi_1 \cos\theta_1 & \rho_1 V_{S1} (1 - 2\sin^2\phi_1) & 2\rho_2 V_{S2} \sin\phi_2 \cos\theta_2 & \rho_2 V_{S2} (1 - 2\sin^2\phi_2) \\ -\rho_1 V_{P1} (1 - 2\sin^2\phi_1) & \rho_1 V_{S1} \sin 2\phi_1 & \rho_2 V_{P2} (1 - 2\sin^2\phi_2) & -\rho_2 V_{S2} \sin 2\phi_2 \end{bmatrix},$$

$$\mathbf{R} = \begin{bmatrix} \sin\theta_1 & \cos\phi_1 & -\sin\theta_2 & -\cos\phi_2 \\ \cos\theta_1 & -\sin\phi_1 & \cos\theta_2 & -\sin\phi_2 \\ 2\rho_1 V_{S1} \sin\phi_1 \cos\theta_1 & \rho_1 V_{S1} (1 - 2\sin^2\phi_1) & 2\rho_2 V_{S2} \sin\phi_2 \cos\theta_2 & \rho_2 V_{S2} (1 - 2\sin^2\phi_2) \\ \rho_1 V_{P1} (1 - 2\sin^2\phi_1) & -\rho_1 V_{S1} \sin 2\phi_1 & -\rho_2 V_{P2} (1 - 2\sin^2\phi_2) & \rho_2 V_{S2} \sin 2\phi_2 \end{bmatrix},$$

where θ_1 , θ_2 , ϕ_1 and ϕ_2 are angles of incidence and refraction for P-waves and S-waves respectively (Aki & Richards 1980). The density, S and P-wave velocities are given by ρ , V_S , and V_P , with the upper and lower media denoted by numbers 1 then 2 (Aki & Richards 1980).

3.2 Anisotropic Zoeppritz Equations

The Zoeppritz equations for an anisotropic system are significantly more complex, comprising of four key stages and requiring the solution to multiple eigenvalue problems (Schoenberg & Protazio 1990). This section outlines the theoretical steps used to develop an efficient three-dimensional anisotropic Zoeppritz modelling code (Schoenberg & Protazio 1990). The only condition required by this formulation is that the media possess at least monoclinic symmetry, defined by an elastic tensor of the following form (Schoenberg & Protazio 1990):

$$\mathbf{C}_{ij} = \begin{bmatrix} C_{11} & C_{12} & C_{13} & & & C_{16} \\ C_{12} & C_{22} & C_{23} & & & C_{26} \\ C_{13} & C_{23} & C_{33} & & & C_{36} \\ & & & C_{44} & C_{45} & \\ & & & C_{45} & C_{55} & \\ C_{16} & C_{26} & C_{36} & & & C_{66} \end{bmatrix}.$$

3.2.1 Incident Slowness Vectors

Step one was to determine the slowness vector of the incident wave, achieved by multiplying equation 8 by V^2/ρ (Haase & Ursenbach 2007). This yielded an eigenvalue problem to find V^2 (Haase & Ursenbach 2007):

$$(\boldsymbol{\Lambda}^U - V^2 \mathbf{I}) \mathbf{q} = 0. \quad (10)$$

$\boldsymbol{\Lambda}^U$ is defined as follows:

$$\begin{aligned} \Lambda_{11}^U &= A_{11}^U n_1^2 + A_{66}^U n_2^2 + A_{55}^U n_3^2 + 2A_{16}^U n_1 n_2 \\ \Lambda_{22}^U &= A_{66}^U n_1^2 + A_{22}^U n_2^2 + A_{44}^U n_3^2 + 2A_{26}^U n_1 n_2 \\ \Lambda_{33}^U &= A_{55}^U n_1^2 + A_{44}^U n_2^2 + A_{33}^U n_3^2 + 2A_{45}^U n_1 n_2 \\ \Lambda_{12}^U &= \Lambda_{21}^U = A_{16}^U n_1^2 + A_{26}^U n_2^2 + A_{45}^U n_3^2 + (A_{12}^U + A_{66}^U) n_1 n_2 \\ \Lambda_{13}^U &= \Lambda_{31}^U = (A_{13}^U + A_{55}^U) n_1 n_3 + (A_{36}^U + A_{45}^U) n_2 n_3 \\ \Lambda_{23}^U &= \Lambda_{32}^U = (A_{36}^U + A_{45}^U) n_1 n_3 + (A_{23}^U + A_{44}^U) n_2 n_3, \end{aligned}$$

where $A_{ij}^U = C_{ij}^U / \rho^U$, $n_i = V s_i$ and U denotes that the incident wave is travelling in the upper medium (Haase & Ursenbach 2007). \mathbf{n} is the unit vector parallel to the wave-front normal, expressed as

$$\mathbf{n} = (n_1, n_2, n_3) = (\cos\phi \sin\theta, \sin\phi \sin\theta, \cos\theta)$$

where ϕ is the azimuth angle and θ is the incident angle (Haase & Ursenbach 2007). The eigenvalues of equation 10, V^2 , were calculated by assuming a non-zero \mathbf{q} :

$$|\boldsymbol{\Lambda}^U - V^2 \mathbf{I}| = 0. \quad (11)$$

The largest eigenvalue corresponds to the P-wave velocity squared, V_P^2 ; the intermediate is the first arriving quasi S-wave velocity squared, V_S^2 ; the smallest is the last arriving quasi S-wave velocity squared, V_T^2 (Schoenberg & Protazio 1990). The three possible incident slowness vectors were then defined as follows (Haase & Ursenbach 2007):

$$\mathbf{s}_P = \left[\frac{n_1}{V_P}, \frac{n_2}{V_P}, \frac{n_3}{V_P} \right], \quad (12)$$

$$\mathbf{s}_S = \left[\frac{n_1}{V_S}, \frac{n_2}{V_S}, \frac{n_3}{V_S} \right], \quad (13)$$

$$\mathbf{s}_T = \left[\frac{n_1}{V_T}, \frac{n_2}{V_T}, \frac{n_3}{V_T} \right]. \quad (14)$$

3.2.2 Reflected and Transmitted Slowness Vectors

The horizontal components of the reflected/transmitted slowness vectors are equal to those of the incident slowness vector due to the constancy of horizontal slowness (Schoenberg & Protazio 1990). The vertical component, s_3 , was calculated by inserting the horizontal slowness components into equation 8 (Haase & Ursenbach 2007). By assuming non-trivial solutions, this yielded the following two equations for the reflected and transmitted slowness vectors, denoted by U and L respectively (Haase & Ursenbach 2007):

$$|\boldsymbol{\Gamma}^U - \rho^U \mathbf{I}| = 0, \quad (15)$$

$$|\boldsymbol{\Gamma}^L - \rho^L \mathbf{I}| = 0. \quad (16)$$

Equations 15 and 16 are bicubic equations in s_3 , each with the following six solutions:

$$\pm\sqrt{s_{3P}^2}, \quad \pm\sqrt{s_{3S}^2}, \quad \pm\sqrt{s_{3T}^2}.$$

The correct wave types were chosen according to the relation

$$\text{Re}(s_{3P}^2) < \text{Re}(s_{3S}^2) < \text{Re}(s_{3T}^2)$$

where Re denotes the real component (Schoenberg & Protazio 1990). The 6 reflected and transmitted slowness vectors were then defined as follows:

$$\mathbf{s}_{PP}^U = \left[\frac{n_1}{V_P}, \frac{n_2}{V_P}, +s_{3P}^U \right], \quad (17)$$

$$\mathbf{s}_{PS}^U = \left[\frac{n_1}{V_S}, \frac{n_2}{V_S}, +s_{3S}^U \right], \quad (18)$$

$$\mathbf{s}_{PT}^U = \left[\frac{n_1}{V_T}, \frac{n_2}{V_T}, +s_{3T}^U \right], \quad (19)$$

$$\mathbf{s}_{PP}^L = \left[\frac{n_1}{V_P}, \frac{n_2}{V_P}, +s_{3P}^L \right], \quad (20)$$

$$\mathbf{s}_{PS}^L = \left[\frac{n_1}{V_S}, \frac{n_2}{V_S}, +s_{3S}^L \right], \quad (21)$$

$$\mathbf{s}_{PT}^L = \left[\frac{n_1}{V_T}, \frac{n_2}{V_T}, +s_{3T}^L \right], \quad (22)$$

where the first P denotes an incident P-wave in this case, followed by either a P , S or T depending on the reflected/transmitted wave type (Schoenberg & Protazio 1990). The impedance matrices \mathbf{X} and \mathbf{Y} account for the sign of the vertical slowness components, so the positive value of s_3 was always applied (Schoenberg & Protazio 1990).

3.2.3 Polarization Vectors

The reflected and transmitted slowness vectors, along with their corresponding layer densities, were inserted into equation 8 (Haase & Ursenbach 2007). This resulted in 6 eigenvalue equations, each with only one unknown: the polarization vector, \mathbf{q} (Haase & Ursenbach 2007). The densities are the eigenvalues and the polarization vectors are their corresponding eigenvectors (Schoenberg & Protazio 1990). The sign of the polarization vectors were chosen so that their horizontal components, q_1 , have the same sign as the corresponding horizontal slowness components, s_1 (Aki & Richards 1980). The polarization vectors were then normalized as follows (Haase & Ursenbach 2007):

$$\|\mathbf{q}\|_2 = q_1^2 + q_2^2 + q_3^2 = 1. \quad (23)$$

3.2.4 Reflection and Transmission Coefficients

Finally, the three-dimensional anisotropic Zoeppritz equations were formulated (Schoenberg & Protazio 1990):

$$\mathbf{R} = (\mathbf{X}_U^{-1} \mathbf{X}_L - \mathbf{Y}_U^{-1} \mathbf{Y}_L) (\mathbf{X}_U^{-1} \mathbf{X}_L + \mathbf{Y}_U^{-1} \mathbf{Y}_L)^{-1}, \quad (24)$$

$$\mathbf{T} = 2 (\mathbf{X}_U^{-1} \mathbf{X}_L + \mathbf{Y}_U^{-1} \mathbf{Y}_L)^{-1}. \quad (25)$$

\mathbf{R} and \mathbf{T} are the reflection and transmission matrices, defined as follows (Schoenberg & Protazio 1990):

$$\mathbf{R} = \begin{bmatrix} R_{PP} & R_{SP} & R_{TP} \\ R_{PS} & R_{SS} & R_{TS} \\ R_{PT} & R_{ST} & R_{TT} \end{bmatrix},$$

$$\mathbf{T} = \begin{bmatrix} T_{PP} & T_{SP} & T_{TP} \\ T_{PS} & T_{SS} & T_{TS} \\ T_{PT} & T_{ST} & T_{TT} \end{bmatrix}.$$

\mathbf{X} and \mathbf{Y} are the impedance matrices, defined for the upper medium as follows (Schoenberg & Protazio 1990):

$$\mathbf{X}_U = \begin{bmatrix} q_{P1}^U & q_{S1}^U & q_{T1}^U \\ q_{P2}^U & q_{S2}^U & q_{T2}^U \\ -(C_{13}^U q_{P1}^U + C_{36}^U q_{P2}^U) s_1^U & -(C_{13}^U q_{S1}^U + C_{36}^U q_{S2}^U) s_1^U & -(C_{13}^U q_{T1}^U + C_{36}^U q_{T2}^U) s_1^U \\ -(C_{23}^U q_{P2}^U + C_{36}^U q_{P1}^U) s_2^U & -(C_{23}^U q_{S2}^U + C_{36}^U q_{S1}^U) s_2^U & -(C_{23}^U q_{T2}^U + C_{36}^U q_{T1}^U) s_2^U \\ -C_{33}^U q_{P3}^U s_{3P}^U & -C_{33}^U q_{S3}^U s_{3S}^U & -C_{33}^U q_{T3}^U s_{3T}^U \\ -(C_{55}^U s_1^U + C_{45}^U s_2^U) q_{P3}^U & -(C_{55}^U s_1^U + C_{45}^U s_2^U) q_{S3}^U & -(C_{55}^U s_1^U + C_{45}^U s_2^U) q_{T3}^U \\ -(C_{55}^U q_{P1}^U + C_{45}^U q_{P2}^U) s_{3P}^U & -(C_{55}^U q_{S1}^U + C_{45}^U q_{S2}^U) s_{3S}^U & -(C_{55}^U q_{T1}^U + C_{45}^U q_{T2}^U) s_{3T}^U \\ -(C_{45}^U s_1^U + C_{44}^U s_2^U) q_{P3}^U & -(C_{45}^U s_1^U + C_{44}^U s_2^U) q_{S3}^U & -(C_{45}^U s_1^U + C_{44}^U s_2^U) q_{T3}^U \\ -(C_{45}^U q_{P1}^U + C_{44}^U q_{P2}^U) s_{3P}^U & -(C_{45}^U q_{S1}^U + C_{44}^U q_{S2}^U) s_{3S}^U & -(C_{45}^U q_{T1}^U + C_{44}^U q_{T2}^U) s_{3T}^U \\ q_{P3}^U & q_{S3}^U & q_{T3}^U \end{bmatrix},$$

$$\mathbf{Y}_U = \begin{bmatrix} q_{P3}^U & q_{S3}^U & q_{T3}^U \end{bmatrix}.$$

The impedance matrices for the lower medium simply require replacing U for L in \mathbf{X}_U and \mathbf{Y}_U (Schoenberg & Protazio 1990).

In case \mathbf{Y}_U , \mathbf{X}_U or both are singular, equations 24 and 25 were reformulated accordingly (Schoenberg & Protazio 1990):

$$\mathbf{R} = (\mathbf{X}_U^{-1} \mathbf{X}_L \mathbf{Y}_L^{-1} \mathbf{Y}_U + \mathbf{I})^{-1} (\mathbf{X}_U^{-1} \mathbf{X}_L \mathbf{Y}_L^{-1} \mathbf{Y}_U - \mathbf{I}), \quad (26)$$

$$\mathbf{T} = 2\mathbf{Y}_L^{-1} \mathbf{Y}_U (\mathbf{X}_U^{-1} \mathbf{X}_L \mathbf{Y}_L^{-1} \mathbf{Y}_U + \mathbf{I})^{-1}, \quad (27)$$

$$\mathbf{R} = (\mathbf{I} + \mathbf{Y}_U^{-1} \mathbf{Y}_L \mathbf{X}_L^{-1} \mathbf{X}_U)^{-1} (\mathbf{I} - \mathbf{Y}_U^{-1} \mathbf{Y}_L \mathbf{X}_L^{-1} \mathbf{X}_U), \quad (28)$$

$$\mathbf{T} = 2\mathbf{X_L}^{-1}\mathbf{X_U} (\mathbf{I} + \mathbf{Y_U}^{-1}\mathbf{Y_L}\mathbf{X_L}^{-1}\mathbf{X_U})^{-1}. \quad (29)$$

$$\mathbf{R} = (\mathbf{Y_L}^{-1}\mathbf{Y_U} + \mathbf{X_L}^{-1}\mathbf{X_U})^{-1} (\mathbf{Y_L}^{-1}\mathbf{Y_U} - \mathbf{X_L}^{-1}\mathbf{X_U})^{-1}, \quad (30)$$

$$\mathbf{T} = 2\mathbf{Y_L}^{-1}\mathbf{Y_U} (\mathbf{Y_L}^{-1}\mathbf{Y_U} + \mathbf{X_L}^{-1}\mathbf{X_U})^{-1} \mathbf{X_L}^{-1}\mathbf{X_U}. \quad (31)$$

3.3 Buzzard Parameter Estimation

In order to model the top-chalk interface using Zoeppritz equations, sensible parameters were first estimated, including minimum and maximum values. These are presented in Table 2. The P-wave velocity of both layers was taken from the starting velocity model in Figure 1. The density of the Clastic Unit was estimated using Gardner's relation (Gardner et al. 1974):

$$\rho = 0.31 V_P^{0.25}. \quad (32)$$

The Chalk Group has a more complex geological history, with evidence of deep burial and over-pressure at depths of 4000m, followed by two episodes of uplift and erosion (Doré & Robbins 2005, Japsen 1998). Therefore, its density was estimated using

$$\rho = \rho_m (1 - \psi) + \rho_f \psi \quad (33)$$

with a porosity, ψ , of 5% determined from a porosity-depth relationship in North Sea chalk samples (Mallon & Swarbrick 2002); a matrix density, ρ_m , of 2710kgm^{-3} (the density of calcite); and fluid density, ρ_f , of 1000kgm^{-3} . The S-wave velocity of the Clastic Unit was estimated from a relationship between P and S-wave velocities in sandstones (DeMartini & Glinsky 2006). Finally, the Chalk Group S-wave velocity was estimated from V_P/V_S ratios of North Sea chalk samples (Røgen et al. 2005). All estimated parameters are given in Table 2.

Vertical transverse isotropy (VTI) is a type of anisotropy with one, vertically oriented axis of symmetry (Thomsen 1986). It is typically defined by three dimensionless anisotropy parameters, δ , ε and γ , known as the Thomsen parameters (Thomsen 1986). The contractors' VTI anisotropy model is given in Table 2. Unlike the starting P-wave velocity model, it has not been verified. Minimum and maximum Thomsen parameters were thus estimated for the top-chalk interface, ignoring the contractors' VTI anisotropy model in case it is incorrect. The use of Thomsen anisotropy parameters constrained the anisotropy to VTI (Thomsen 1986). This was a reasonable initial constraint, as it is the most frequently encountered type of anisotropy in geophysical applications (Thomsen 1986). The elastic tensor of a VTI medium is related to the Thomsen parameters and the P and S-wave velocities that define the medium by the following exact expressions (Thomsen 1986):

$$V_P = \sqrt{C_{33}/\rho}, \quad (34)$$

$$V_S = \sqrt{C_{44}/\rho}, \quad (35)$$

$$\varepsilon \equiv \frac{C_{11} - C_{33}}{2C_{33}}, \quad (36)$$

$$\gamma \equiv \frac{C_{66} - C_{44}}{2C_{44}}, \quad (37)$$

$$\delta \equiv \frac{1}{2} \left[\varepsilon + \frac{\delta^*}{(1 - V_P^2/V_S^2)} \right]. \quad (38)$$

δ^* is defined as:

$$\delta^* \equiv \frac{1}{2C_{33}^2} [2(C_{13} + C_{44})^2 - (C_{13} - C_{44})(C_{11} + C_{33} - 2C_{44})]. \quad (39)$$

The range of δ and ε values that have been explored are shown in Table 2. They were chosen from Thomsen (1986) and are in the weak to moderate range, i.e. $\delta, \varepsilon \leq 0.2$. S-wave anisotropy was not analysed in this study, therefore γ was neglected. The magnitude and nature of the anisotropy cannot be constrained further without the addition of extra a priori information.

Parameter	Clastic Unit			Chalk Group		
	min.	ass.	max.	min.	ass.	max.
V_P (m/s)	-	2000	-	-	4000	-
V_S (m/s)	200	400	600	1800	2150	2500
ρ (kg/m ³)	1800	2000	2200	2400	2600	2800
	CR			CR		
δ	-0.1	0.04	0.2	-0.1	0.025	0.2
ε	-0.02	0.08	0.2	-0.02	0.05	0.2

Table 2: Estimated parameters for the Buzzard top-chalk interface. V_P minima and maxima were not estimated as the assumed values have been verified. The contractors' anisotropy model is denoted by CR and the range of anisotropy that has been explored is given by the minimum and maximum values.

3.4 Monte Carlo Simulations

As the estimated parameters are poorly constrained, Monte Carlo simulations were employed to fully investigate the range of possible reflection coefficient profiles from the top-chalk interface. The distributions of the simulated reflection coefficients at discrete angles of incidence were also analysed. The Zoeppritz equations, along with effective computer implementation, allow for almost instantaneous computation of reflection coefficients; Monte Carlo methods take full advantage of this.

An elastic isotropic simulation was conducted by generating 1000 uniformly distributed random samples between the minimum and maximum for V_S and ρ in Table 2. These samples, as well as the assumed V_P , were then used to forward model 1000 random P-wave reflection coefficient profiles using the isotropic Zoeppritz Modelling Code.

The estimated anisotropic parameter space constrains the maximum potential magnitude and type of anisotropy (VTI), but does not constrain its specific nature. Elastic anisotropic simulations were therefore conducted with all other parameters held constant to assess the sensitivity of the system to anisotropy alone. 1000 uniformly distributed random samples were generated between the minimum and maximum values for δ and ε in Table 2. This approach takes full account of the non-correlation between δ and ε discussed in Thomsen (1986). To fully assess the impact of anisotropy on the P-wave reflection coefficients, the isotropic parameters were chosen from Table 2 so that the elastic effects were minimised i.e. using maximum Clastic Unit and minimum Chalk Group values. Two elastic anisotropic simulations were initially conducted: one with an anisotropic Clastic Unit and an isotropic Chalk Group, the other with a fully anisotropic system.

4 Results

4.1 Zoepritz Modelling Code

4.1.1 Functionality

A comprehensive code for modelling anisotropic elastic media in three dimensions using Zoepritz equations has been developed in Python 3, referred to as the Zoepritz Modelling Code (ZMC). The code is provided as a supplementary material and its key sections are given in Appendix A.1. It generates reflection/transmission coefficient profiles and an accompanying phase shift at angles of incidence ranging from 0° to 90° in a specified azimuth across an interface between two homogenous elastic anisotropic media. The only condition is that both media must possess monoclinic or higher symmetries (Schoenberg & Protazio 1990). The input for the program requires the densities of both media, the elastic tensors (in 6×6 notation) of both media, the azimuth of the incident wave and the type of coefficient required to plot (e.g. R_{PP} or T_{PS}). The ZMC is configured assuming the incident wave is a P-wave arriving in the upper medium, however modification is straightforward if required. As illustrated in Figure 5, the ZMC can also plot reflection coefficient profiles against offset given the interface depth.

The ZMC is highly vectorised, utilising the Walt et al. (2011) high performance scientific computing package NumPy; it takes 0.0025 seconds to compute a single reflection coefficient. An implementation of the Aki & Richards (1980) isotropic Zoepritz matrix equation has also been developed in Python, see Appendix A.2. This is faster than the anisotropic version (ZMC) by a factor of 10, an advantage when performing very large Monte Carlo simulations.

4.1.2 Development

Developing an accurate and robust anisotropic Zoepritz modelling program is a non-trivial task (Schoenberg & Protazio 1990). Numerous flaws were debugged throughout each stage of the code's development. Two crucial problems that arose are summarised in this section, along with their corresponding solutions. As shown in Table 3, the code has been validated using two exact plane-wave P-wave reflection coefficient solutions taken from Figure 2 and Figure 4 in Rüger (1997) and shown in Table 3. Figure 2's solution is for an isotropic incident medium and a VTI reflecting medium, whilst Figure 4's is for an isotropic incident medium and a HTI reflecting medium at varying azimuths (Rüger 1997).

The first crucial problem was the entire failure of the program for isotropic and transversely isotropic media. Impedance matrices \mathbf{X} and \mathbf{Y} have been formulated for monoclinic media (Schoenberg & Protazio 1990), however in an isotropic or transversely isotropic elastic tensor, the following components and their diagonally reflected values are zero: C_{16} , C_{26} , C_{36} , C_{45} (Thomsen 1986). This caused the impedance matrices to become singular and the program to fail, despite the multiple inversion strategies presented in section 3.2.4. To solve this, a very small amount of whitening was added to the elastic tensors relative to their magnitudes:

$$\mathbf{C}_{ij} = \mathbf{C}_{ij} + \mu \|\mathbf{C}_{ij}\|_F \quad (40)$$

where F denotes the Frobenius norm and the whitening factor, μ , was experimentally chosen to be 1×10^{-7} .

As shown in Figure 4, the second major problem was the significant instabilities in phase at incidence angles greater than 40° and reflection coefficients beyond the equivalent elastic critical angle at 69° . The reflection coefficients and the phase fluctuated between two solutions. This was caused by the incorrect handling of the complex valued reflected/transmitted vertical slowness components, s_3 . To fix this, both imaginary and real components of s_3 were removed if they were below a magnitude of $1 \times 10^{-6} \text{sm}^{-1}$, where they can be considered insignificant. The positive sign convention for imaginary s_3 was then enforced (Schoenberg & Protazio 1990). The corrected result is also displayed in Figure 4.

VTI Test					
Incidence Angle	0°	10°	20°	30°	40°
Exact R_{PP}	0.038	0.042	0.055	0.080	0.127
Calculated R_{PP}	0.03789	0.04189	0.05471	0.07971	0.12768

HTI Test					
Incidence Angle	40°	40°	40°	40°	-
Azimuth Angle	0°	30°	60°	90°	-
Exact R_{PP}	0.096	0.087	0.071	0.065	-
Calculated R_{PP}	0.09538	0.08660	0.07143	0.06512	-

Table 3: Zoeppritz Modelling Code validation against exact plane-wave P-wave reflection coefficient solutions taken from Figure 2 (VTI Test) and Figure 4 (HTI Test) in Rüger (1997). Note that the exact solutions could only be measured from the plots in Rüger (1997) at an accuracy of 0.001.

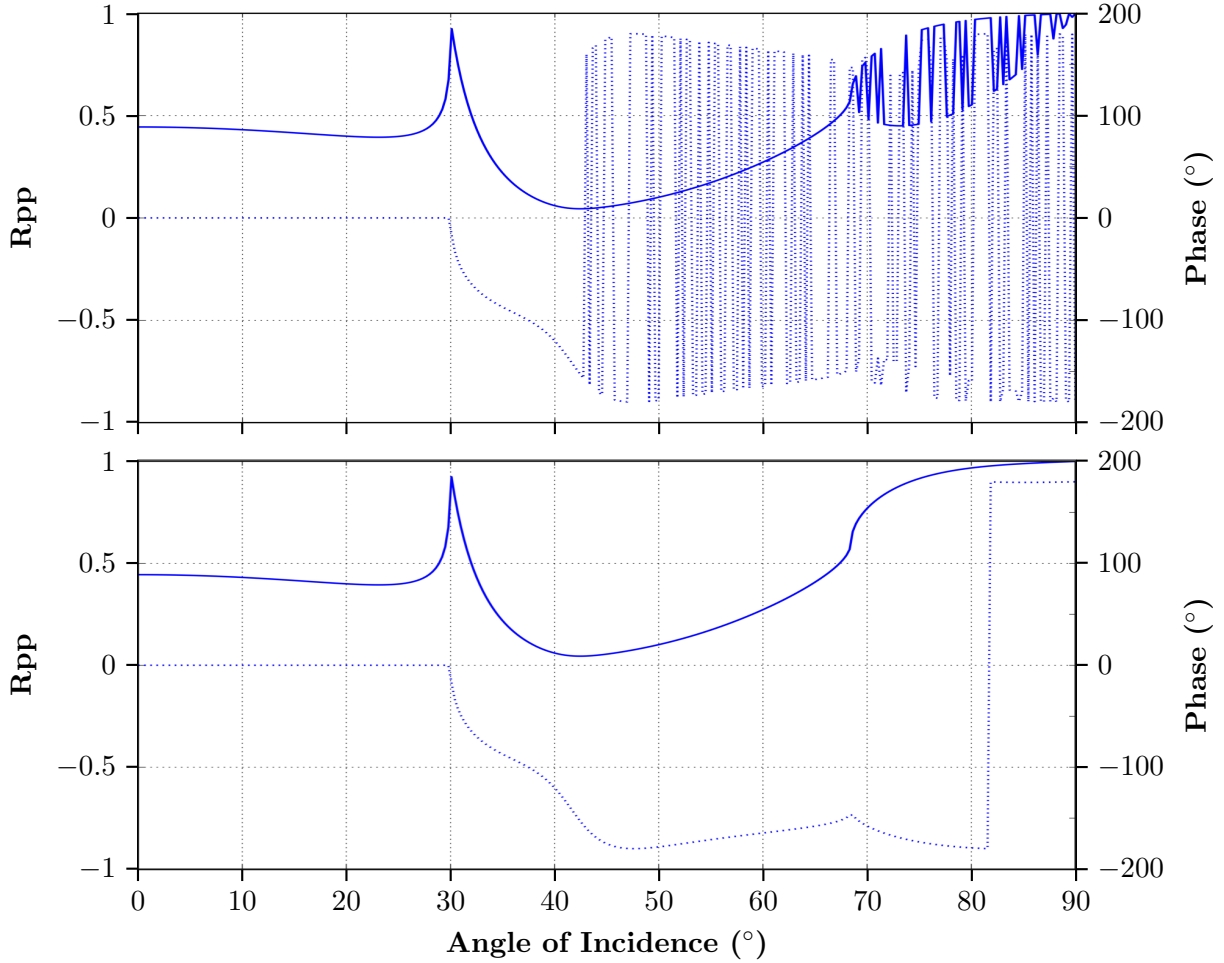


Figure 4: Top: reflection coefficient and phase profile exhibiting severe instabilities prior to code fix. Bottom: same profile produced by the corrected Zoeppritz modelling code. The assumed elastic isotropic parameters in Table 2 were used. Note that the sudden jump in phase at approximately 82° is meaningless as a -180° phase shift is the same as $+180^{\circ}$ phase shift.

4.2 Buzzard Zoeppritz Modelling

P-wave reflection coefficient profiles for the top-chalk interface in the Buzzard Field were generated using the ZMC. Figure 5 illustrates the isotropic acoustic ($V_S = 0$) and elastic profiles. The critical angle occurs at 30° , or at 1150m offset. At pre-critical angles the reflection coefficients are relatively similar. However, at post-critical angles there is a significant disparity between the acoustic and elastic reflection coefficients, with an immediate reduction in the elastic coefficients ($R_{PP} = 0.1$), whereas total reflection occurs for the acoustic case ($R_{PP} = 1$). The elastic post-critical reflection coefficients then steadily rise from 0.1 to 0.51 over offsets ranging from 1800m to 5000m. Including the contractors' anisotropy model introduced negligible changes to the elastic profile.

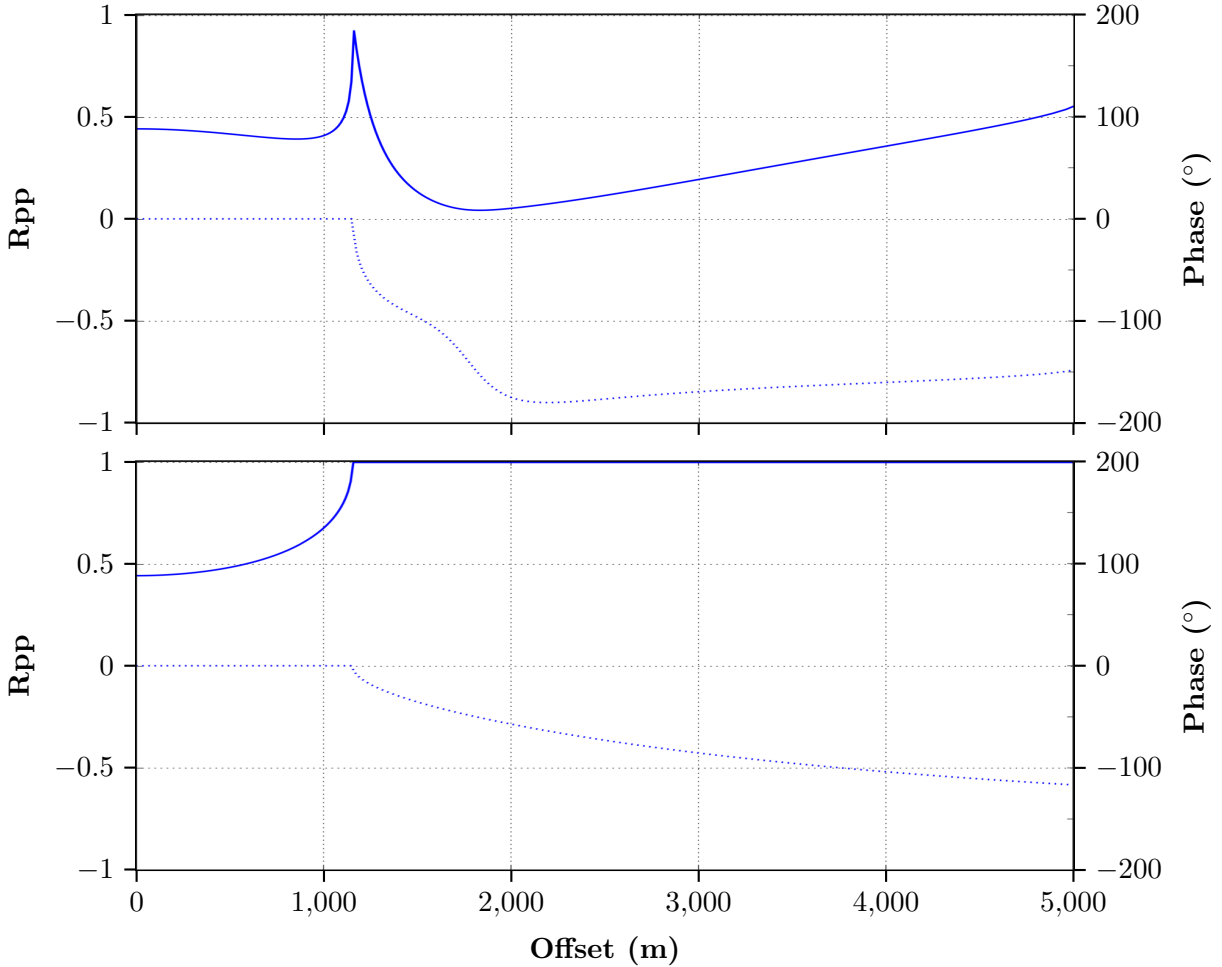


Figure 5: P-wave reflection coefficient and phase profiles from the Buzzard top-chalk interface, using the assumed isotropic parameters from Table 2. Top: elastic profile. The solid line represents the P-wave reflection coefficient (R_{PP}), and the dotted line represents the phase. Bottom: acoustic profile ($V_S = 0$).

4.3 Buzzard Monte Carlo Simulations

4.3.1 Isotropic Simulation

The isotropic elastic Monte Carlo simulation and probability density functions at incidence angles of 15° , 45° and 75° are shown in Figure 6. The reduction in elastic post-critical P-wave reflection coefficients observed in Figure 5 is present for all 1000 simulated profiles and is most significant at incidence angles of 45° . At pre-critical incidence angles, the reflection coefficients are concentrated in a narrow, bell-shaped distribution with a mode of approximately 0.4. Post-critical reflection coefficients at angles of incidence ranging from 35° to 50° are concentrated below 0.2. This is illustrated by the positively skewed distribution and extremely low mode of 0.05 at an incidence angle of 45° . Beyond angles of 55° , there is a bimodal distribution of reflection coefficients. This is displayed in the 75° probability density function and is a consequence of the equivalent elastic critical angle that arises when the S-wave velocity of the Chalk Group exceeds the P-wave velocity of the Clastic Unit. Note that the high reflection coefficients exhibited at incidence angles greater than 68° are at offsets exceeding 5km, putting them beyond (or very close to) the end of the survey.

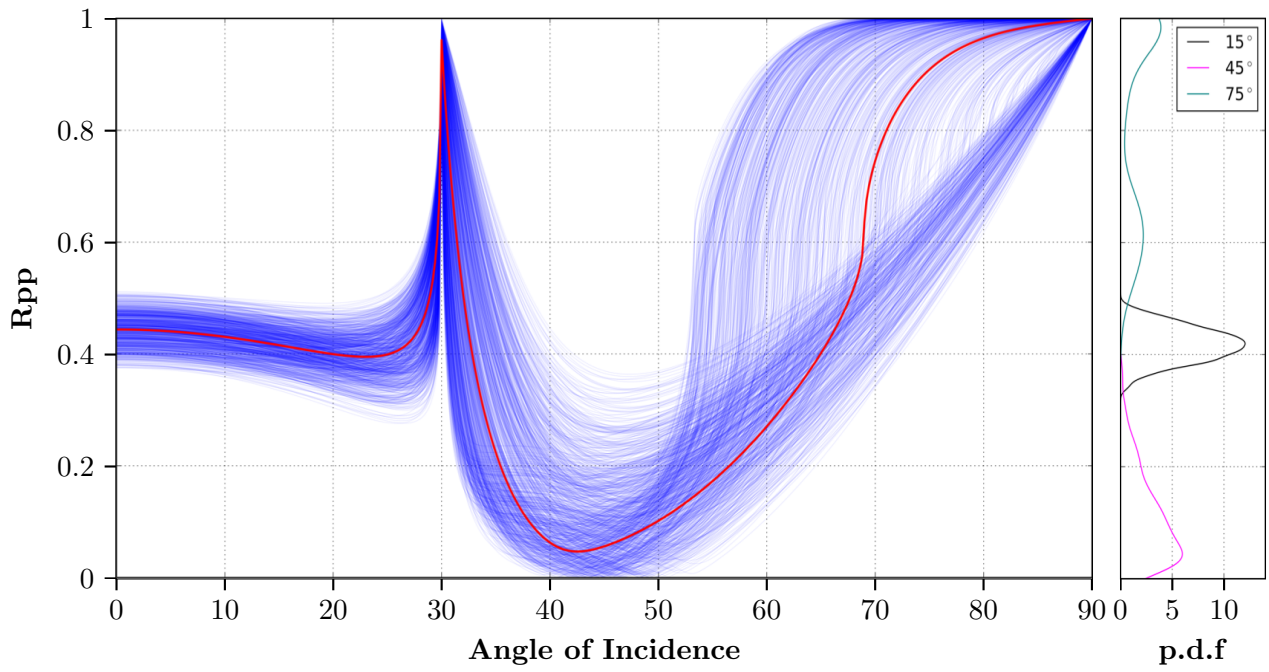


Figure 6: Isotropic elastic Monte Carlo simulation (left) and corresponding probability density functions at incidence angles of 15° , 45° , 65° (right). The blue lines represent the simulated P-wave reflection coefficient profiles using the estimated isotropic parameter ranges in Table 2. The red profile illustrates the assumed result, using the assumed isotropic parameters in Table 2.

4.3.2 Anisotropic Simulations

The anisotropic elastic Monte Carlo simulation, assuming an anisotropic Clastic Unit and an isotropic Chalk Group, is presented in Figure 7, with the fully anisotropic elastic Monte Carlo simulation presented in Figure 8. The reflection coefficients in Figure 7 are narrowly distributed at each incidence angle, with a range that does not exceed 0.2. In contrast, at post-critical incidence angles between 30° and 60° in Figure 8, there is a wide distribution of reflection coefficients. The 45° probability density function illustrates this, ranging from 0.15 to 0.75. More precisely, it was found that the post-critical P-wave reflection coefficients are reduced relative to the isotropic case if $\delta < \varepsilon$ in the Chalk Group; this reduction is large if $\varepsilon - \delta \geq 0.2$. For instance, if $\delta = -0.05$ and $\varepsilon = 0.2$ in the Chalk Group, the P-wave reflection coefficient at an angle of incidence of 40° is reduced from the isotropic value of 0.5 to 0.1. Also note that a positive ε value reduces the critical angle and vice versa; the maximum estimated ε value of 0.2 in the lower layer causes a critical angle reduction of 5° .

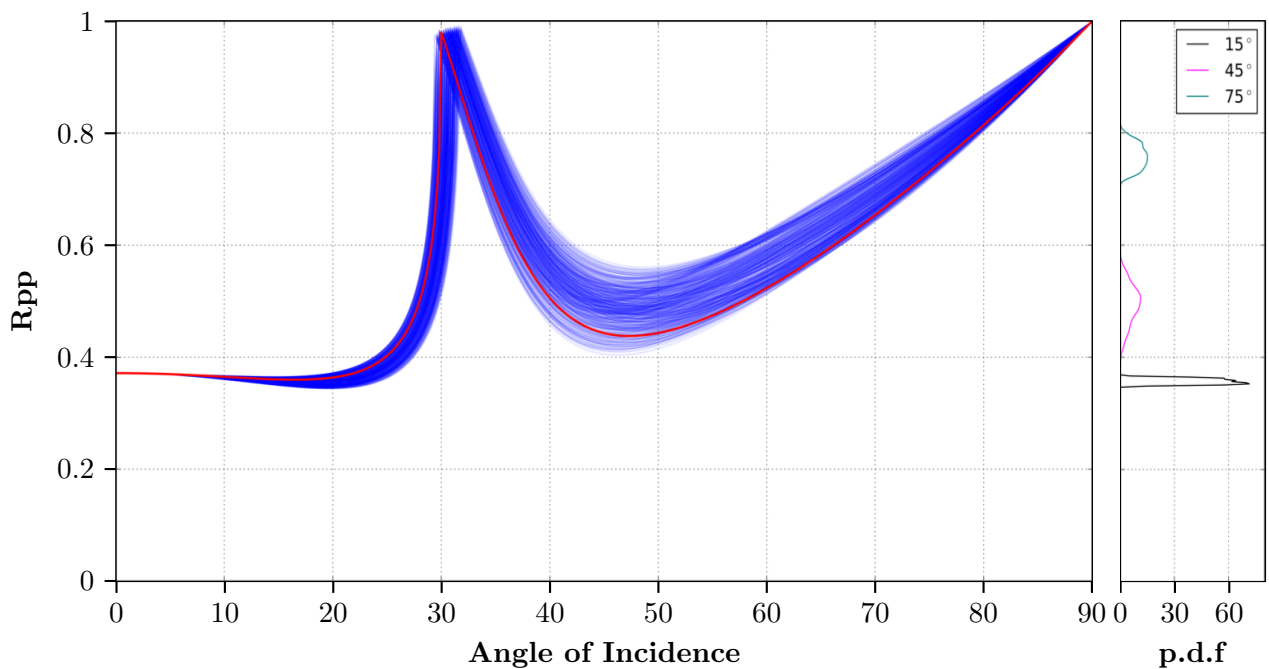


Figure 7: Anisotropic Monte Carlo simulation assuming an anisotropic Clastic Unit and an isotropic Chalk Group (left) and corresponding probability density functions at incidence angles of 15° , 45° , 65° (right). The blue lines represent the simulated P-wave reflection coefficient profiles using the estimated range of δ and ε in the Clastic Unit, the minimum isotropic Chalk Group parameters and the maximum isotropic Clastic Unit parameters from Table 2. The red profile represents the fully isotropic case.

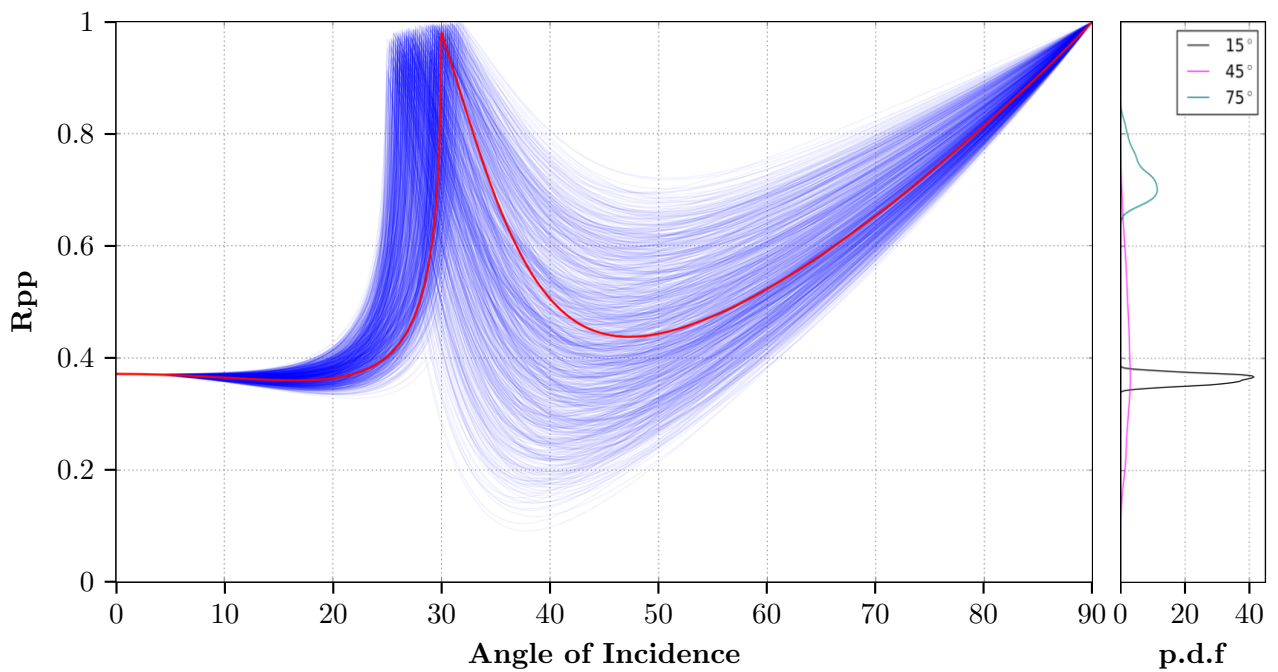


Figure 8: Fully Anisotropic Monte Carlo simulation (left) and corresponding probability density functions at incidence angles of 15° , 45° , 65° (right). The blue lines represent the simulated P-wave reflection coefficient profiles using the estimated ranges of δ and ε , the minimum isotropic Chalk Group parameters and the maximum isotropic Clastic Unit parameters from Table 2. The red profile represents the fully isotropic case.

5 Discussion

5.1 Kirchhoff Synthetic Seismogram

The Zoeppritz equations assume seismic energy travels in rays with infinite frequency (Zoeppritz 1919). However, seismic waves have finite frequencies and accounting for this will effectively average out the reflection coefficient profile over the Fresnel zone (Aki & Richards 1980). The Zoeppritz Modelling Code also does not take geometrical spreading into consideration (Schoenberg & Protazio 1990). To account for these effects and model the reflected wave-field from the top-chalk interface, an additional code was developed that generates Kirchhoff synthetic seismograms from P-wave reflection coefficients (see Appendix A.3) (Shearer 2009).

The Kirchhoff program computes the reflected wave-field from a flat, horizontal interface between two media by utilising the tangent plane hypotheses (Shearer 2009), an approximation which states that the reflected wave-field immediately above the interface is given by the Zoeppritz P-wave reflection coefficient for the incident ray (Scott & Helmberger 1983). The reflected wave-field for a specific receiver, ϕ_R , was calculated using a Kirchhoff integral of the form

$$\phi_R = \frac{1}{4\pi c} \int_S \delta \left(t - \frac{r + r_0}{c} \right) \frac{R_{PP}(\theta_0)}{rr_0} (\cos \theta_0 + \cos \theta) dS * \frac{\partial w(t, f)}{\partial t}, \quad (41)$$

where c is the P-wave velocity of the incident medium, δ is the Dirac delta function, $R_{PP}(\theta_0)$ is the plane-wave P-wave reflection coefficient at incidence angle θ_0 , r_0 and r are the source to surface grid-point and surface grid-point to receiver distances respectively, θ is the angle between the scattered ray and the surface normal, w is the source time function and the integral is conducted over surface S (Shearer 2009). A Ricker wavelet was used as the source time function, w , defined as follows (Ricker 1943):

$$w(t, f) = (1 - 2\pi^2 f^2 t^2) e^{-\pi^2 f^2 t^2}. \quad (42)$$

For post-critical incidence angles equation 41 becomes complex, requiring an additional phase shift (Shearer 2009). Therefore, the final Kirchhoff synthetic seismogram was given by

$$\phi_R = \text{Re}(\phi_R) + H \{ \text{Im}(\phi_R) \} \quad (43)$$

where H is the Hilbert transform, and the real and imaginary components are denoted by Re and Im respectively (Shearer 2009).

Kirchhoff synthetic seismograms for the Buzzard top-chalk interface are shown in Figure 9. They were generated at a frequency of 10Hz, the same frequency employed in the Buzzard FWI, using the

same isotropic acoustic and elastic reflection coefficients from Figure 5. The disparity between the acoustic and elastic post-critical reflection coefficients is well defined in the Kirchhoff synthetics; the elastic amplitudes are reduced to less than 0.1 at offsets between 1500m and 3000m, whereas the acoustic synthetic exhibits large amplitudes throughout. Additionally, the gradual increase observed in the elastic post-critical reflection coefficients is suppressed by the effects of geometrical spreading at offsets greater than 3000m. Also note that the sharp spike in elastic reflection coefficients at the critical angle has been averaged over the Fresnel zone in the Kirchhoff synthetic and is therefore not observed (Aki & Richards 1980). The same model was used to generate acoustic and elastic synthetics using the FWI numerical wave equation solver (equation 1), as shown in Appendix B.2. The same behaviour in amplitude and phase are present, supporting previous results and observations.

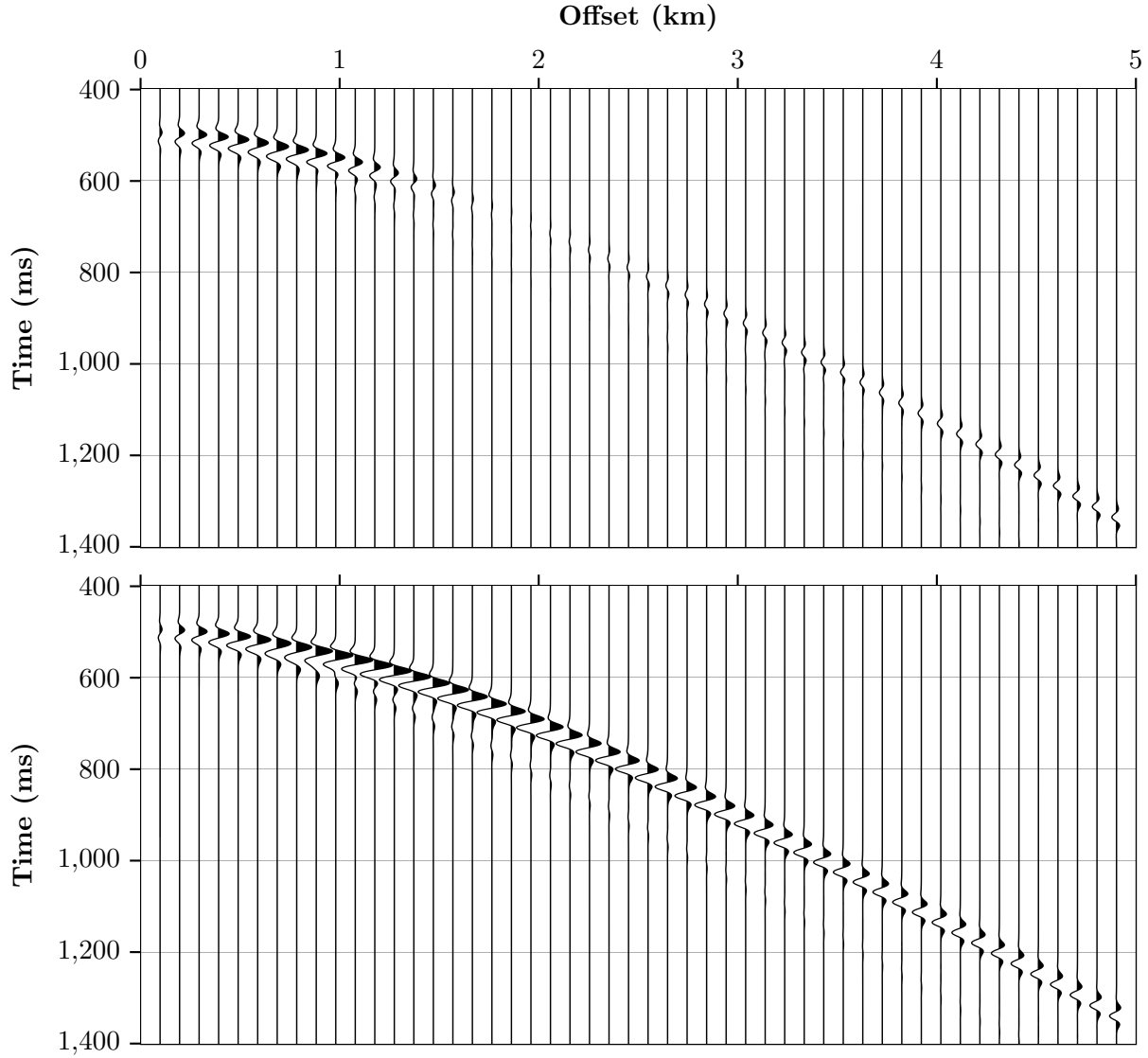


Figure 9: Kirchhoff synthetic seismograms for the Buzzard top-chalk interface, using the assumed isotropic parameters from Table 2. Top: elastic Kirchhoff synthetic. Bottom: acoustic Kirchhoff synthetic ($V_S = 0$). A scale factor of 2 has been applied to all traces.

5.2 Elastic Effects

Isotropic Zoeppritz modelling of the Buzzard top-chalk interface, presented in Figure 5, has shown that elastic effects cause a large reduction in post-critical P-wave reflection coefficients. The isotropic elastic Monte Carlo simulation (Figure 6) demonstrates that this phenomenon occurs for all possible model configurations within the estimated parameter space. Moreover, the reduction in reflection coefficients is severe in most cases, as illustrated by the positively skewed distribution of reflection coefficients at an incidence angle of 45° . This phenomenon propagates directly into the reflected wavefield, dominating the elastic Kirchhoff synthetic (Figure 9).

The Buzzard field data and acoustic synthetic from Figure 3 were revisited in order to compare post-critical top-chalk reflections with the Kirchhoff synthetics. To remove the direct arrivals, which strongly overprint the top-chalk post-critical reflections, an F-K filter has been applied and the resultant records are shown in Figure 10. The post-critical top-chalk reflections in Figure 10 exhibit the same disparity in amplitude displayed by the Kirchhoff elastic and acoustic synthetics.

The impact of the elastic effects are further enhanced by the shallow depth of the Chalk Group, which causes the early arriving multiples that dominate the acoustic synthetic in Figure 10. The acoustic post-critical top-chalk reflection coefficients are 1 and so little energy is lost in their multiples, whereas the elastic post-critical top-chalk reflection coefficients are approximately 0.1; their multiples have practically negligible energy. Using a free-surface P-wave reflection coefficient of 1, the relative seismic amplitudes of the 1st, 2nd and 3rd order multiples are all 1 for the acoustic case, and 0.01, 0.001 and 0.0001 for the elastic case respectively. It was thus hypothesised that elastic effects, originating from the top-chalk interface, are responsible for the failure of acoustic FWI on the Buzzard field data set.

Acoustic FWI has been successfully applied to numerous North Sea data sets containing chalk formations that typically occur at depths of approximately 3000m, 2000m deeper than the Buzzard chalk (Liu et al. 2012, Warner et al. 2013, Ratcliffe et al. 2011). In these cases, the top-chalk post-critical elastic effects may still be present, but are inconsequential as they appear off the end of the survey. It has therefore been hypothesized that elastic effects are likely to cause the failure of acoustic FWI on data sets where a sharp interface with significant P and S-wave velocity contrasts is present at shallow depths ($< 1500\text{m}$). This situation is likely to arise where chalk, salt, igneous, metamorphic or carbonate rocks have experienced significant uplift.

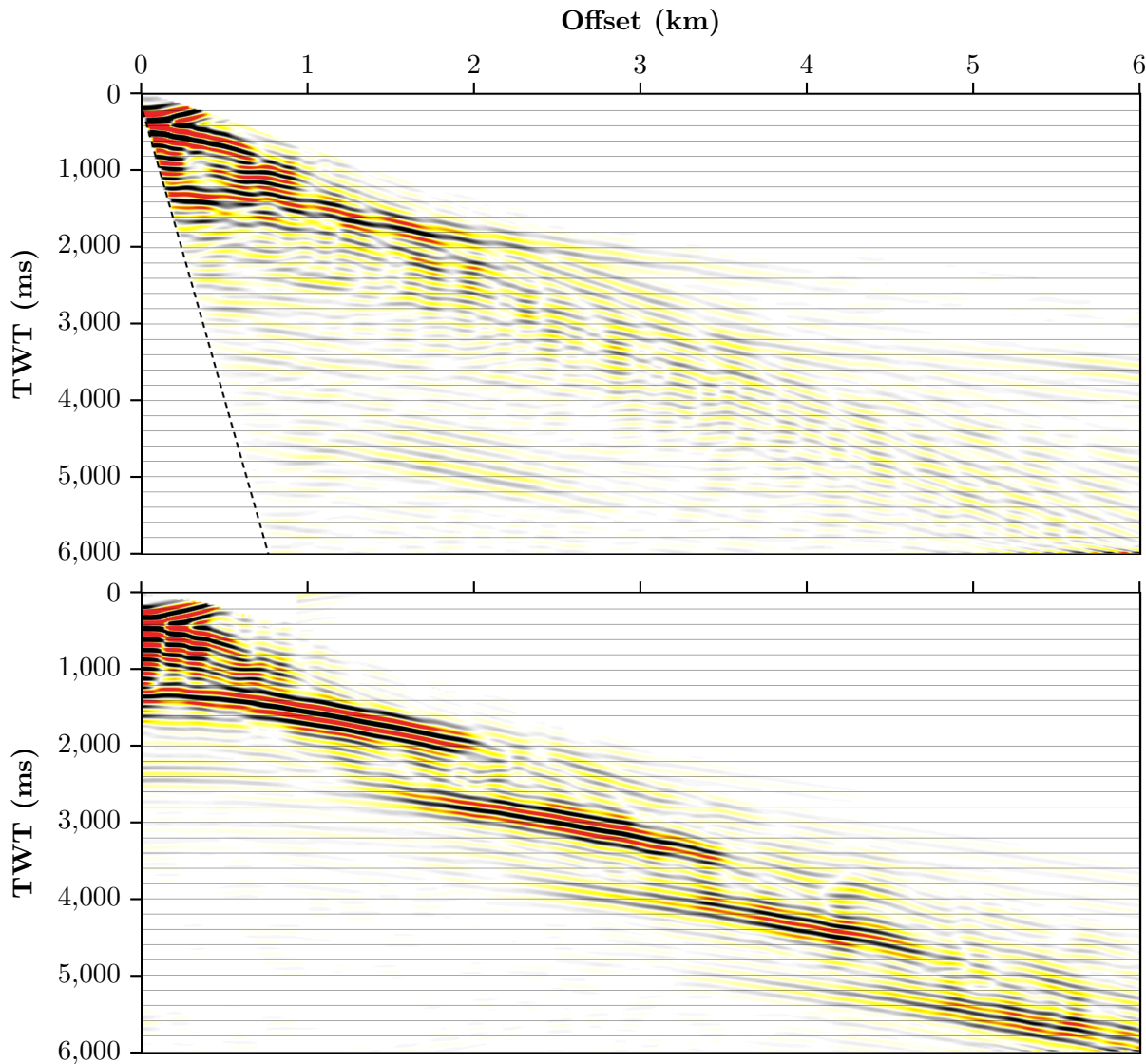


Figure 10: Top: F-K filtered shot record of the Buzzard field data from Figure 3. The dotted black line indicates where a mute was applied to remove Scholte waves. Bottom: F-K filtered acoustic synthetic from Figure 3. The post-critical top-chalk reflections, which were heavily overprinted by direct arrivals in Figure 3, are well illustrated.

5.3 Anisotropic Effects

Anisotropic Zoeppritz modelling of the Buzzard top-chalk interface showed that the P-wave reflection coefficients were practically unaltered by incorporating the contractors' anisotropy model. The first anisotropic Monte Carlo simulation (Figure 7) is consistent with this result; the narrow distribution of reflection coefficients throughout the simulated profiles demonstrates that the P-wave reflection coefficients are insensitive to weak anisotropy within the Clastic Unit. However, the fully anisotropic Monte Carlo simulation in Figure 8 shows that the post-critical reflection coefficients are highly sensitive to weak anisotropy in the Chalk Group. This is illustrated by the wide distribution of reflection coefficients at angles of incidence ranging from 30° to 60°.

Due to its depositional nature, it is highly probable that there is vertical transverse isotropy due to layering of isotropic materials within the Clastic Unit (Thomsen 1986, Doré & Robbins 2005). The presence of anisotropy within the Chalk Group is less certain. Moderate VTI anisotropy, $\varepsilon = 0.2$ and $\delta = 0.07$, has previously been assigned to the Ekofisk chalk formation in the North Sea, yet this was deemed unlikely due to the lithological properties of chalk (Warner et al. 2013). However, significant (up to 30%) azimuthal anisotropy has been confirmed in multiple chalk formations, for instance: the Valhall, Fife and Ekofisk chalks in the North Sea (Hall & Kendall 2003, Li 1999, Barton 2007); and the Austin chalk, Texas (Leary et al. 1990). This has been attributed to the presence of near-vertical, aligned fractures (Hall & Kendall 2003, Li 1999, Barton 2007, Leary et al. 1990). This type of anisotropy can be modelled by horizontal transverse isotropy (HTI) (Thomsen 1995): transverse isotropy with a horizontal axis of symmetry. Due to its complex geological history and the high density of East-West trending faults in the Buzzard field (Doré & Robbins 2005), it is much more probable that the Chalk Group has HTI anisotropy due to the alignment of vertical fractures.

By utilising the Bond transformation matrix, a VTI elastic tensor can be rotated 90° about a horizontal axis, yielding a HTI elastic tensor with the same magnitude of anisotropy, but in a different orientation (Bond 1943). The equation required for rotation about the x_2 axis is

$$\mathbf{C}_{ij}^R = \mathbf{MC}_{ij}\mathbf{M}^T \quad (44)$$

where \mathbf{C}_{ij}^R is the rotated elastic tensor and \mathbf{M} is the Bond transformation matrix for rotation angle ζ , defined as follows (Bond 1943):

$$\mathbf{M} = \begin{bmatrix} \cos^2\zeta & 0 & \sin^2\zeta & 0 & -\sin 2\zeta & 0 \\ 0 & 1 & 0 & 0 & 0 & 0 \\ \sin^2\zeta & 0 & \cos^2\zeta & 0 & \sin 2\zeta & 0 \\ 0 & 0 & 0 & \cos\zeta & 0 & \sin\zeta \\ 0.5\sin 2\zeta & 0 & -0.5\sin 2\zeta & 0 & \cos 2\zeta & 0 \\ 0 & 0 & 0 & -\sin\zeta & 0 & \cos\zeta \end{bmatrix}.$$

This facilitates the modelling of the top-chalk interface with VTI anisotropy in the Clastic Unit and HTI anisotropy in the Chalk Group. As shown in Figure 11, Monte Carlo simulations have been conducted to assess the behaviour and sensitivity of reflection coefficients at azimuths of 0° , 30° , 60° and 90° to HTI anisotropy in the Chalk Group, with the same parameters used for the previous anisotropic simulation in Figure 8.

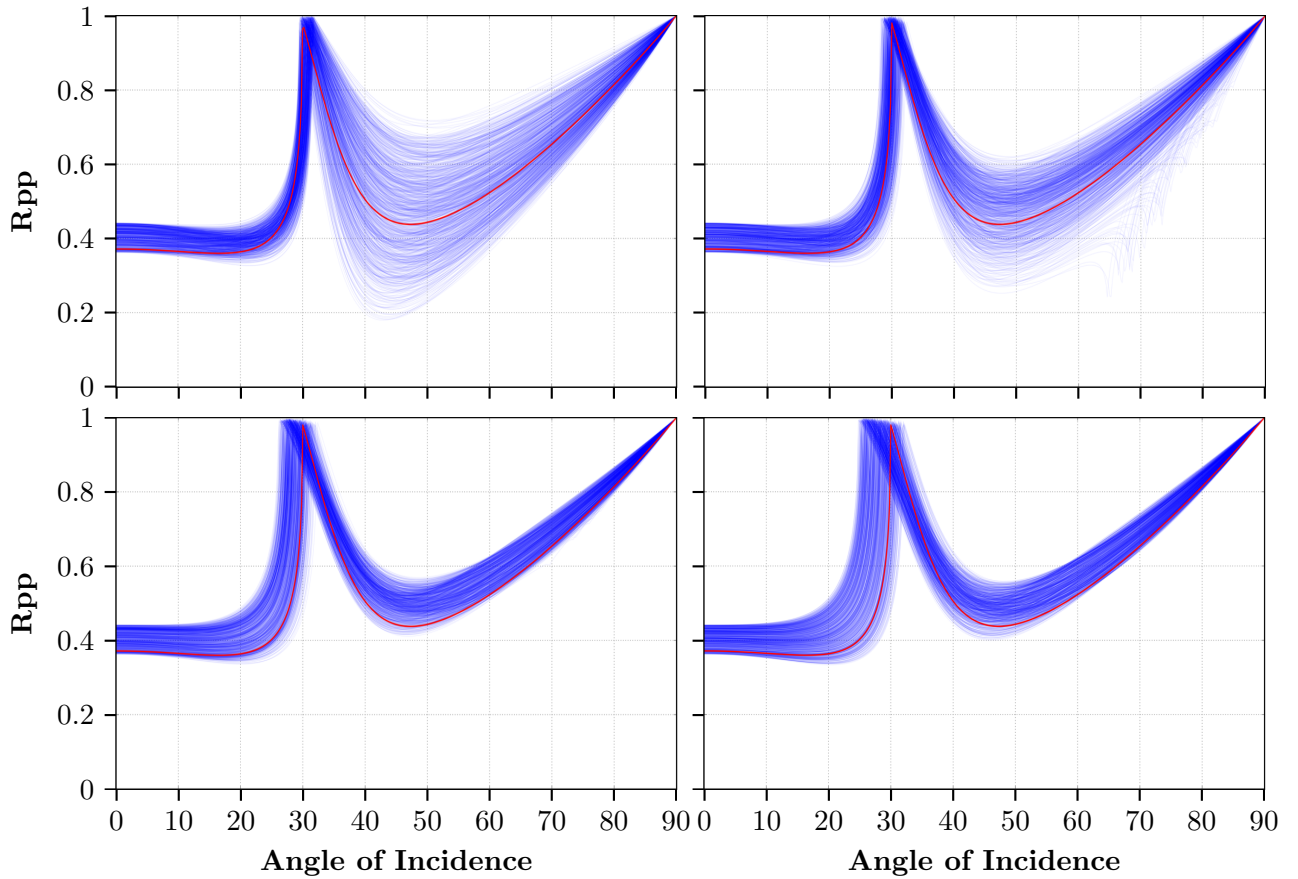


Figure 11: HTI anisotropic Monte Carlo simulations at azimuths of 0° (top-left), 30° (top-right), 60° (bottom-left) and 90° (bottom-right). These were generated using the estimated ranges of δ and ε , the minimum isotropic Chalk Group parameters and the maximum isotropic Clastic Unit parameters from Table 2 (the same as in Figure 8). HTI anisotropy in the Chalk Group was achieved using the 90° bond transformation. The red profile represents the fully isotropic case.

Figure 11 illustrates that the sensitivity of the post-critical reflection coefficients to HTI anisotropy in the Chalk Group vary distinctly with azimuth. At 0° , perpendicular to the fracture alignment

and horizontal axis of symmetry, the post-critical reflection coefficients are highly sensitive to HTI anisotropy in the Chalk Group. However, at azimuths of 90° - parallel to the fracture alignment and horizontal axis of symmetry - and 60° , the post-critical reflection coefficients are completely insensitive to HTI anisotropy in the Chalk Group. The residual post-critical distribution is purely a result of the VTI anisotropy in the Clastic Unit. Note that the post-critical reflection coefficients in the HTI case are still reduced most significantly when the Chalk Group has parameters $\varepsilon - \delta \geq 0.2$ prior to Bond transformation.

Assuming that the elastic effects are not as significant as predicted and that the contractors' anisotropy model is incorrect, it is possible that moderate anisotropy in the Chalk Group can considerably reduce the post-critical P-wave reflection coefficients (Figure 8). However, VTI anisotropy is unlikely to be present within chalk (Warner et al. 2013) and HTI anisotropy can only significantly reduce the post-critical reflection coefficients at azimuths approximately perpendicular to the fracture alignment. As the FWI was performed in 3D on full-azimuth OBN seismic data and fails consistently across the whole data set, HTI anisotropy is unlikely to be responsible. Therefore, anisotropy has been discounted as a cause for the failure of acoustic FWI on the Buzzard field data set.

Although anisotropy was not the problem in the Buzzard FWI, this study has highlighted its potential impact. For instance, the VTI anisotropic Monte Carlo simulation in Figure 8 revealed that the post-critical P-wave reflection coefficients are greatly reduced if $\varepsilon - \delta \geq 0.2$ in the reflecting medium. It is well known that fine layering of isotropic media produce VTI anisotropy where $\varepsilon - \delta > 0$ (Berryman 1979, Thomsen 1986). Furthermore, it has been shown that numerous materials possess VTI anisotropy where $\varepsilon - \delta \geq 0.2$; for example, the Mesaverde calcareous sandstone and the Green River shale presented in Thomsen (1986). It should also be noted that fully accounting for these effects in the acoustic approximation is not possible even when the elastic effects are practically negligible. This is illustrated by the discrepancy between post-critical reflection coefficients in Appendix B.3. Therefore, acoustic FWI will not correctly handle data sets containing a well defined shallow interface with large contrasts in P-wave velocity (but not necessarily S-wave velocity) in which the reflecting medium possesses anisotropy where $\varepsilon - \delta \geq 0.2$ and it may entirely fail when these effects are combined with moderate elastic effects.

6 Conclusion

The failure of acoustic FWI on the Buzzard field data set was due to the presence of elastic effects originating from the top-chalk interface. These effects caused a severe reduction in the post-critical P-wave reflection coefficients of 90% relative to the acoustic case and their impact was magnified by the Chalk Group's shallow depth of 1000m. This suggests that acoustic FWI will likely fail on data sets due to elastic effects if they contain a well defined shallow interface with similarly large P and S-wave velocity contrasts (2000ms^{-1} and 1700ms^{-1} respectively). The post-critical P-wave reflection coefficients were also shown to be highly sensitive to weak/moderate anisotropy within the Chalk Group. If the elastic effects are not as severe as predicted and the anisotropy of the chalk satisfies $\varepsilon - \delta \geq 0.2$, then the post-critical reflection coefficients are reduced by at least 40%. These effects cannot be fully accounted for in acoustic FWI even when the elastic effects are practically negligible. It was therefore hypothesised that acoustic FWI will not correctly deal with data sets containing a shallow interface, with significant P-wave velocity contrasts, where the anisotropy of the reflecting medium satisfies $\varepsilon - \delta \geq 0.2$.

I have developed a comprehensive code for modelling reflection and transmission coefficients in anisotropic elastic media that is accurate, efficient, and robust. This code was implemented within Monte Carlo simulations to fully explore the parameter space and conduct sensitivity analyses. It has also been used to make an additional program that generates Kirchhoff synthetic seismograms. After the successful use of the Zoeppritz Modelling Code, Monte Carlo simulations and Kirchhoff synthetic seismograms on evaluating why acoustic FWI failed on the Buzzard field data set, it is my intention that they be used to evaluate the effectiveness of acoustic FWI on data sets following failures, provide diagnostics and used prior to FWI to assess whether it will be successful. These methods can also be applied in the future to help solve the complex task, discussed in Warner et al. (2012), of selecting the appropriate physics that need to be incorporated for FWI to be successful in different situations. As elastic effects need to be accounted for to proceed with FWI on the Buzzard field data set, this study ultimately highlights the growing need for elastic FWI (Guasch et al. 2012) or methods for mitigating elastic effects (Agudo et al. 2016) when tackling increasingly more challenging data in the future.

References

- Agudo, O. C., da Silva, N., Warner, M. & Morgan, J. (2016), Acoustic full-waveform inversion in an elastic world, in ‘SEG Technical Program Expanded Abstracts 2016’, Society of Exploration Geophysicists, pp. 1058–1062.
- Aki, K. & Richards, P. (1980), *Quantitative seismology: theory and methods*, Freeman Co., San Francisco.
- Barton, N. (2007), ‘Fracture-induced seismic anisotropy when shearing is involved in production from fractured reservoirs’, *Journal of Seismic Exploration* **16**(2), 115.
- Berryman, J. G. (1979), ‘Long-wave elastic anisotropy in transversely isotropic media’, *Geophysics* **44**(5), 896–917.
- Bond, W. L. (1943), ‘The mathematics of the physical properties of crystals’, *Bell Labs Technical Journal* **22**(1), 1–72.
- DeMartini, D. C. & Glinsky, M. E. (2006), ‘A model for variation of velocity versus density trends in porous sedimentary rocks’, *Journal of Applied Physics* **100**(1), 014910.
- Doré, G. & Robbins, J. (2005), ‘The Buzzard Field’, *Geological Society, London, Petroleum Geology Conference series* **6**(1), 241–252.
- Gardner, G., Gardner, L. & Gregory, A. (1974), ‘Formation velocity and density – The diagnostic basics for stratigraphic traps’, *Geophysics* **39**(6), 770–780.
- Guasch, L., Warner, M., Nangoo, T., Morgan, J., Umpleby, A., Stekl, I. & Shah, N. (2012), ‘Elastic 3D full-waveform inversion’.
- Haase, A. B. & Ursenbach, C. (2007), Plane-wave reflection coefficients for anisotropic media: practical implementation, Technical report, CREWES Research Report.
- Hall, S. A. & Kendall, J.-M. (2003), ‘Fracture characterization at Valhall: Application of P-wave amplitude variation with offset and azimuth (AVOA) analysis to a 3D ocean-bottom data set’, *Geophysics* **68**(4), 1150–1160.
- Japsen, P. (1998), ‘Regional velocity-depth anomalies, North Sea Chalk: a record of overpressure and Neogene uplift and erosion’, *AAPG bulletin* **82**(11), 2031–2074.
- Keith, C. M. & Crampin, S. (1977), ‘Seismic body waves in anisotropic media: Reflection and refraction at a plane interface’, *Geophysical Journal International* **49**(1), 181–208.
- Leary, P. C., Crampin, S. & McEvilly, T. V. (1990), ‘Seismic fracture anisotropy in the Earth’s crust: An overview’, *Journal of Geophysical Research: Solid Earth* **95**(B7), 11105–11114.

- Li, X.-Y. (1999), ‘Fracture detection using azimuthal variation of P-wave moveout from orthogonal seismic survey lines’, *Geophysics* **64**(4), 1193–1201.
- Liu, F., Guasch, L., Morton, S. A., Warner, M., Umpleby, A., Meng, Z., Fairhead, S. & Checkles, S. (2012), 3-D time-domain full waveform inversion of a Valhall OBC dataset, in ‘SEG Technical Program Expanded Abstracts 2012’, Society of Exploration Geophysicists, pp. 1–5.
- Mallon, A. & Swarbrick, R. (2002), ‘A compaction trend for non-reservoir North Sea Chalk’, *Marine and Petroleum Geology* **19**(5), 527–539.
- Ratcliffe, A., Win, C., Vinje, V., Conroy, G., Warner, M., Umpleby, A., Stekl, I., Nangoo, T. & Bertrand, A. (2011), Full waveform inversion: A North Sea OBC case study, in ‘SEG Technical Program Expanded Abstracts 2011’, Society of Exploration Geophysicists, pp. 2384–2388.
- Ray, F. M., Pinnock, S. J., Katamish, H. & Turnbull, J. B. (2011), ‘The Buzzard Field: anatomy of the reservoir from appraisal to production’, *Geological Society, London, Petroleum Geology Conference series* **7**(1), 369–386.
- Ricker, N. (1943), ‘Further developments in the wavelet theory of seismogram structure’, *Bulletin of the Seismological Society of America* **33**(3), 197–228.
- Røgen, B., Fabricius, I. L., Japsen, P., Høier, C., Mavko, G. & Pedersen, J. M. (2005), ‘Ultrasonic velocities of north sea chalk samples: Influence of porosity, fluid content and texture’, *Geophysical Prospecting* **53**(4), 481–496.
- Rüger, A. (1997), ‘P-wave reflection coefficients for transversely isotropic models with vertical and horizontal axis of symmetry’, *Geophysics* **62**(3), 713–722.
- Schoenberg, M. & Protazio, J. (1990), ‘Zoeppritz rationalized, and generalized to anisotropic media’, *The Journal of the Acoustical Society of America* **88**(S1), S46–S46.
- Scott, P. & Helmberger, D. (1983), ‘Applications of the Kirchhoff-Helmholtz integral to problems in seismology’, *Geophysical Journal International* **72**(1), 237–254.
- Seabed-Geosolutions (2014), ‘Acquisition Report: Nexen Buzzard 4D OBN Baseline Survey’.
- Shearer, P. M. (2009), *Introduction to seismology*, Cambridge University Press.
- Tarantola, A. (1984), ‘Inversion of seismic reflection data in the acoustic approximation’, *Geophysics* **49**(8), 1259–1266.
- Thomsen, L. (1986), ‘Weak elastic anisotropy’, *Geophysics* **51**(10), 1954–1966.
- Thomsen, L. (1995), ‘Elastic anisotropy due to aligned cracks in porous rock’, *Geophysical Prospecting* **43**(6), 805–829.

- Virieux, J. & Operto, S. (2009), ‘An overview of full-waveform inversion in exploration geophysics’, *Geophysics* **74**(6), WCC1–WCC26.
- Voigt, W. (1910), *Lehrbuch der Krystallphysik: (mit Ausschluss der Krystalloptik)*, BG Teubner.
- Walt, S. v. d., Colbert, S. C. & Varoquaux, G. (2011), ‘The NumPy array: a structure for efficient numerical computation’, *Computing in Science & Engineering* **13**(2), 22–30.
- Warner, M., Morgan, J., Umpleby, A., Stekl, I. & Guasch, L. (2012), Which physics for full-wavefield seismic inversion?, in ‘74th EAGE Conference and Exhibition incorporating EUROPEC 2012’.
- Warner, M., Ratcliffe, A., Nangoo, T., Morgan, J., Umpleby, A., Shah, N., Vinje, V., tekl, I., Guasch, L., Win, C., Conroy, G. & Bertrand, A. (2013), ‘Anisotropic 3D full-waveform inversion’, *Geophysics* **78**(2), R59–R80.
- Zoeppritz, K. (1919), ‘Erdbebenwellen VIII B, Über Reflexion und Durchgang seismischer wellen durch Unstetigkeitsflächen’, *Gottinger Nachr* **1**, 66–84.

Appendix B Additional Figures

B.1 Contractors' Anisotropy Model

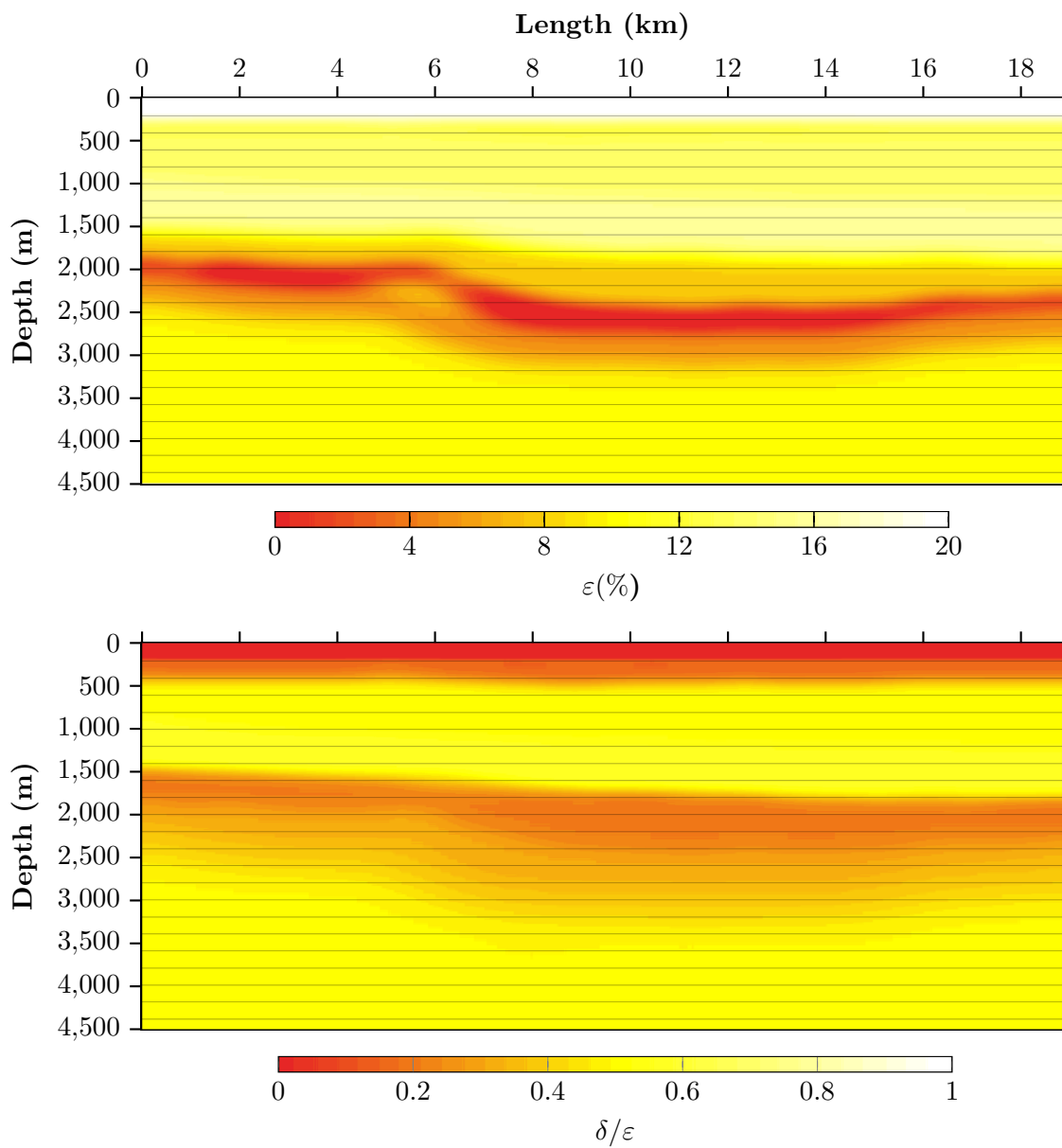


Figure 12: Contractors' VTI anisotropy model. Top: ε model. Bottom: δ/ε model.

B.2 FWI Synthetics

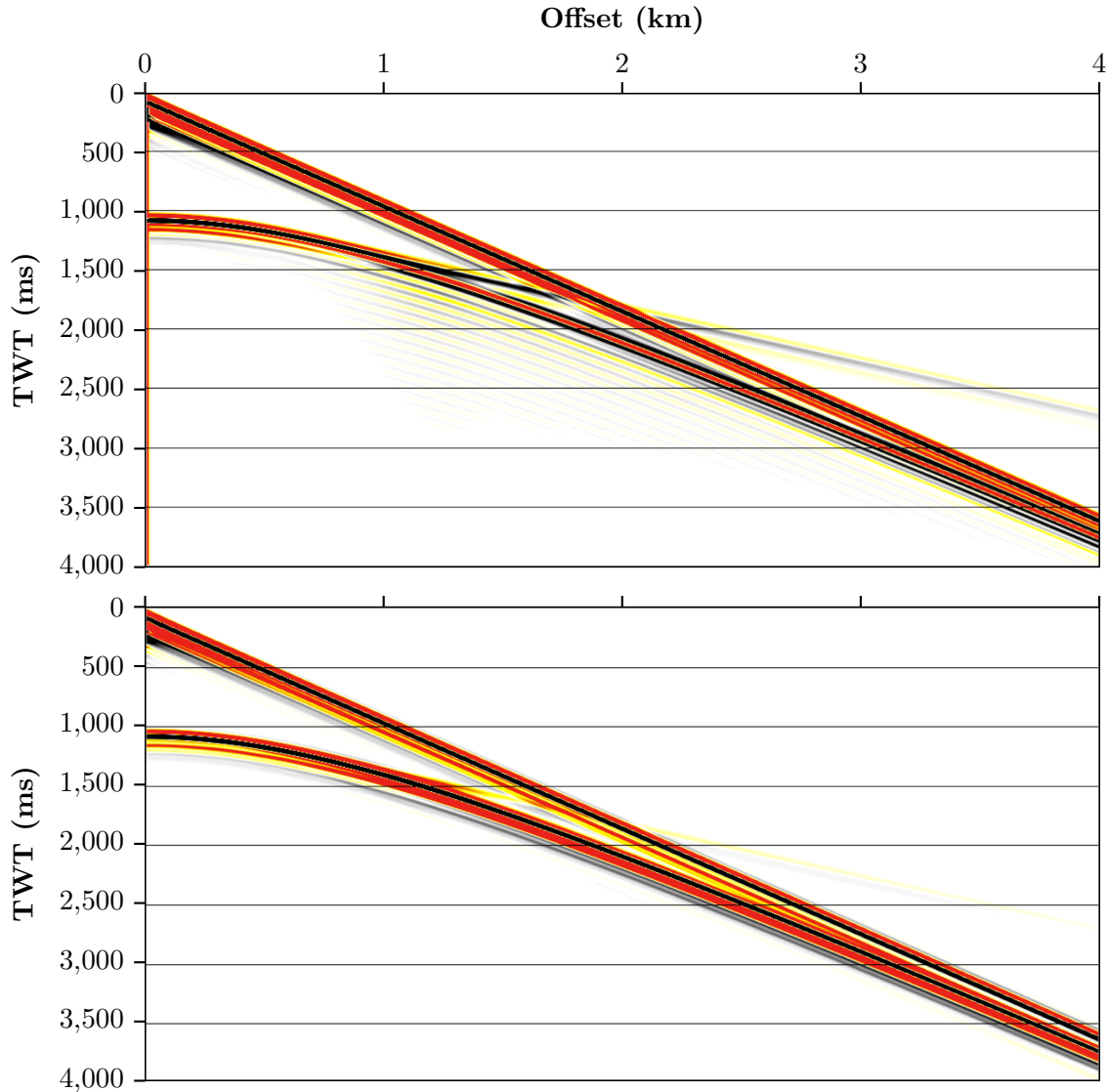


Figure 13: Top: isotropic elastic FWI synthetic data. Bottom: isotropic acoustic FWI synthetic data generated using a homogenous two layer model with the assumed parameters from Table 2. Note the reduction in amplitude and rapid phase shifts of the elastic post-critical reflections. No trace scaling has been applied and both synthetics are plotted at the same amplitude.

B.3 Acoustic Modelling of Anisotropic Effects

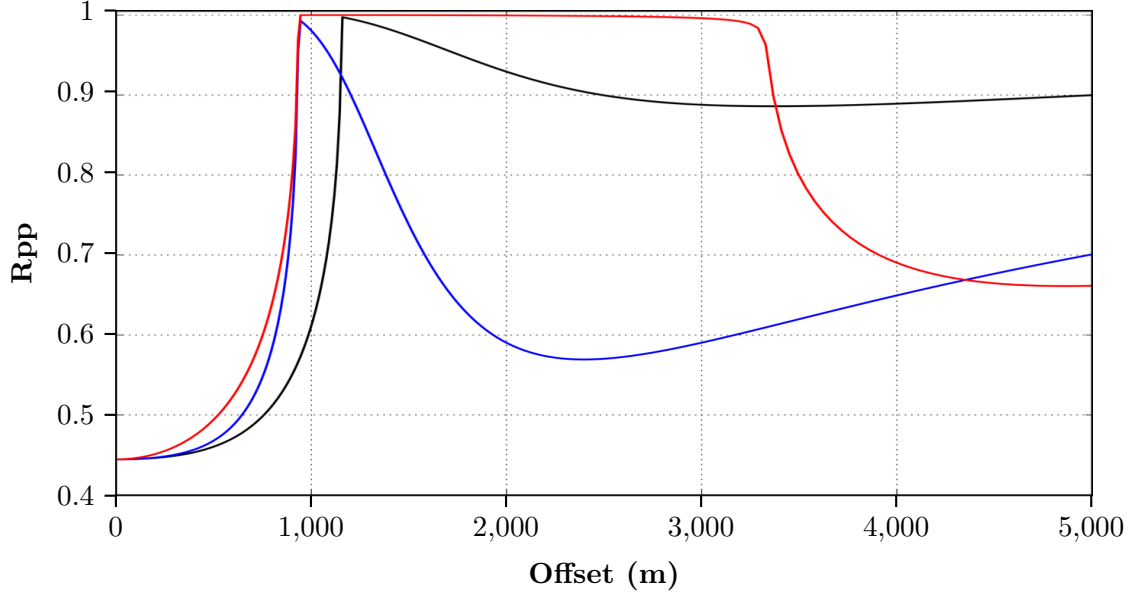


Figure 14: P-wave reflection coefficients for isotropic elastic modelling (black line), anisotropic elastic modelling (blue line), anisotropic acoustic modelling (red line). This was generated using parameters of $V_{P1} = 2000$, $V_{S1} = 1100$, $\rho_1 = 2000$, $\varepsilon_1 = 0$, $\delta_1 = 0$, $V_{P2} = 4000$, $V_{S2} = 1400$, $\rho_2 = 2600$, $\varepsilon_2 = 0.2$, $\delta_2 = 0.03$. Note the significant difference in post-critical reflection coefficients between the elastic anisotropic (blue) and acoustic anisotropic (red) profiles despite very minor elastic effects (black).